Microscopic Imaging and Spectroscopy with Scattered Light

Nada N. Boustany,[1] Stephen A. Boppart,[2] and Vadim Backman[3]

[1]Department of Biomedical Engineering, Rutgers University, Piscataway, New Jersey 08854; email: nboustan@rci.rutgers.edu

[2]Departments of Electrical and Computer Engineering, Bioengineering, and Medicine, Beckman Institute for Advanced Science and Technology, University of Illinois at Urbana-Champaign, Urbana, Illinois 61801; email: boppart@illinois.edu

[3]Department of Biomedical Engineering, McCormick School of Engineering and Applied Science, Northwestern University, Evanston, Illinois 60208; email: v-backman@northwestern.edu

Key Words

light scattering, optical imaging, microscopy, tissue diagnosis, cell analysis

Abstract

Optical contrast based on elastic scattering interactions between light and matter can be used to probe cellular structure, cellular dynamics, and image tissue architecture. The quantitative nature and high sensitivity of light scattering signals to subtle alterations in tissue morphology, as well as the ability to visualize unstained tissue in vivo, has recently generated significant interest in optical-scatter-based biosensing and imaging. Here we review the fundamental methodologies used to acquire and interpret optical scatter data. We report on recent findings in this field and present current advances in optical scatter techniques and computational methods. Cellular and tissue data enabled by current advances in optical scatter spectroscopy and imaging stand to impact a variety of biomedical applications including clinical tissue diagnosis, in vivo imaging, drug discovery, and basic cell biology.

Contents

1. INTRODUCTION

In contrast with X rays, which travel with relatively little scatter through biological tissues, electromagnetic waves at optical wavelengths are significantly scattered at biological interfaces. This scattering of light by optically inhomogeneous biological tissues has posed a limitation on high-resolution, three-dimensional imaging of thick biological tissues and in general has prevented whole-body, optical tomographic imaging on the scale of X-ray computed tomography. Nonetheless, elastic scattering of light at tissue, cellular, and subcellular interfaces provides an important source of natural biological contrast that can be harnessed to provide quantitative measurements of cellular and tissue states. Thus significant advances in optical technology have recently focused on utilizing this fundamental form of light-tissue interaction to enable optical-scatter-based imaging and sensing. High-resolution optical scatter sensing is usually limited to tissue surfaces, thin specimens, or weakly scattering tissues. However, important biomedical and biological applications ranging from cancer diagnosis to cell and developmental biology have been achieved even in this limited scattering regime. This review presents recent advances in optical scatter imaging and spectroscopy and includes a description of novel methodologies and the biological data that can be derived from them.

2. ELASTIC LIGHT SCATTERING AS A SOURCE OF OPTICAL CONTRAST

Aside from absorption by blood and certain tissue pigments (e.g., melanin) in specific wavelength ranges (1), elastic scattering is by far the most prevalent form of light interaction with biological tissue, with elastic scattering cross sections that are several orders of magnitude larger than fluorescence or inelastic Raman scattering.

In contrast with fluorescence, which carries information about the excited energy state of a specific biochemical, elastic scattering does not involve photon absorption, and the atoms involved do not make a transition to an excited state before the scattering process takes place. Because the process is elastic and does not involve absorption (**Figure 1a**), the scattered light has the same frequency as the incident light, and elastic scattering can occur for a broad range of incident wavelengths. (A detailed quantum description of the scattering process can be found in Reference 2.) In a typical measurement, light incident on a scattering source is elastically scattered in different directions upon interaction with the scattering source. By measuring the magnitude, phase, and the angular dependency or wavelength dependency of the scattered far field, one can retrieve information about the scattering sources' cross sections (or extinction resulting from scattering), structure, and refractive index (3). The dependency of scattering on the polarization of the incident field can also be used to study the birefringent or dichroic properties of the scattering source (3, 4). **Figure 1c** shows an illustration of light scatter irradiance as a function of angle and size for two spheres of different diameter (**Figure 1b**). As noted in the figure, the angular intensity depends on the ratio of the particles' refractive index to the surrounding medium's refractive index, and on
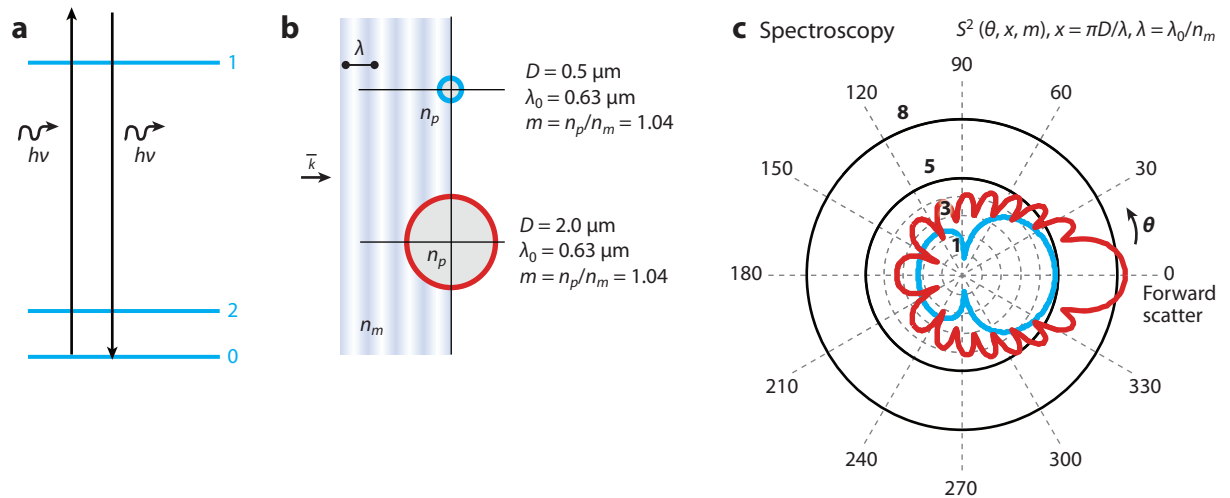

Figure 1

Optical scatter spectroscopy. (*a*) Energy diagram illustration of light-matter interaction based on elastic light scattering. $h\nu$ represents the incident and scattered photon energy. (*b*, *c*) Elastically scattered light can be analyzed as a function of wavelength and scattering angle to extract information about particle size and refractive index. The blue scattergram in panel *c* corresponds to a numerical simulation of light scattering by the small blue sphere in panel *b*; the red scattergram in panel *c* corresponds to the larger red sphere in panel *b*. A plane wave with wavelength $\lambda = \lambda_0/n_m$ is incident on the spheres that have diameter D and refractive index $n_p = 1.38$ and that are located in a medium with refractive index $n_m = 1.33$. m is the refractive index ratio n_p/n_m. $\bar{k}$ is the wavevector indicating the direction of the light wave incident on the spheres. The normalized scattering phase function S^2, corresponding to the scattering intensity, is plotted as a function of polar scattering angle θ between the scattered and incident directions. The magnitude of S^2 varies as a function of radial position on this polar plot and is shown for $S^2 = 1, 3, 5, 8$.
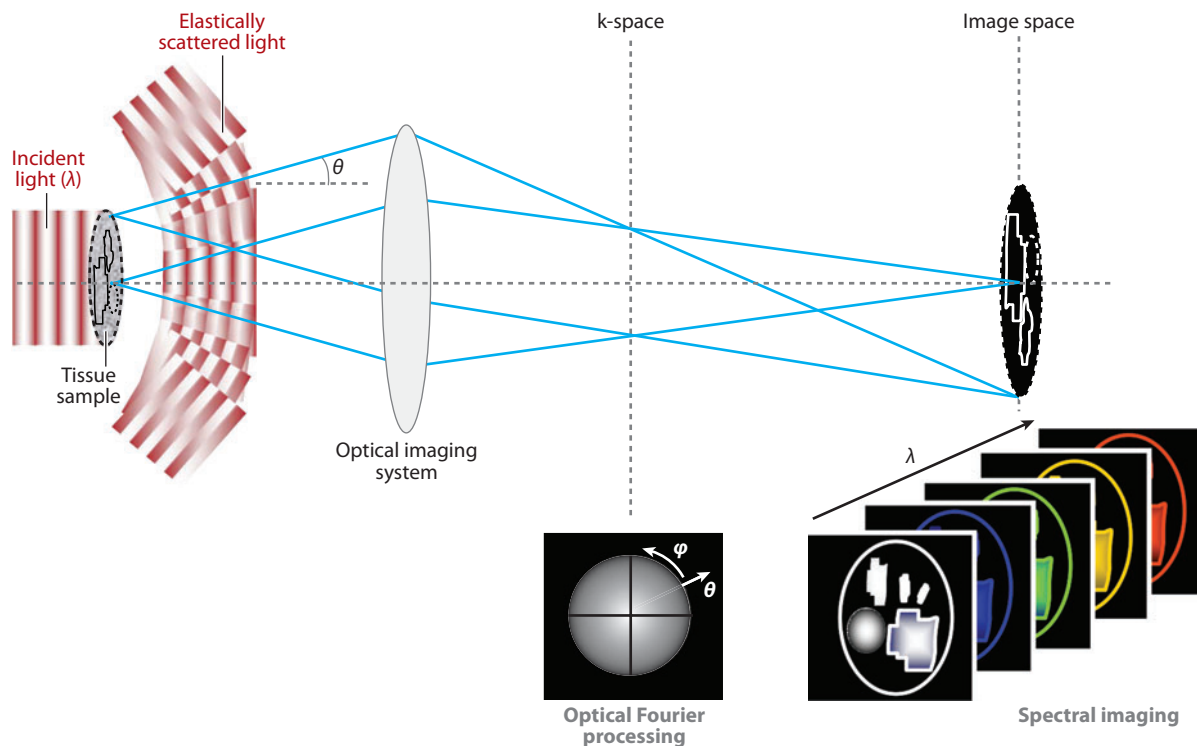
Figure 2

Wide-field or scanning confocal microscopy. Elastic light scattering measurements collected in a transmission-imaging configuration. Similar data can be collected in a reflectance configuration. θ, polar scattering angle; φ, azimuthal angle.

the ratio of the particle diameter to the wavelength of the incident light. The scattering signal can be measured spectroscopically as a function of angle and wavelength as illustrated in **Figure 1c**. However, if the data are acquired with an imaging system (**Figure 2**), the elastic scattering signal can be spatially registered with the positions of the corresponding scattering sources, resulting in optical scatter maps (images) of the sample. In this case, researchers can obtain the spectral dependency of the scattering signal by varying the wavelength of the incident light used to image the sample, whereas they can retrieve the angular scattering data from a conjugate transform plane of the imaging system. Finally, interferometry can be used to obtain the light scattering information (**Figure 3**) in order to quantify phase-sensitive scattering.

3. PHYSICAL INTERPRETATION OF THE OPTICAL SCATTER DATA

Rayleigh scattering by electrical dipoles constitutes a fundamental form of elastic scattering by individual biological molecules or biological particles with dimensions much smaller than the wavelength of the light. However, biological tissue consists of many different compartments with different indices of refraction. These compartments range in size and may have dimensions and separation distances on the order of—or smaller than—the wavelength of light. For example, organelles within cells may be as large as half a micron or as small as a few tens of nanometers, and they may be separated from other organelles by distances on the order of less than one micron to several microns. These biological compartments are too large to scatter like individual
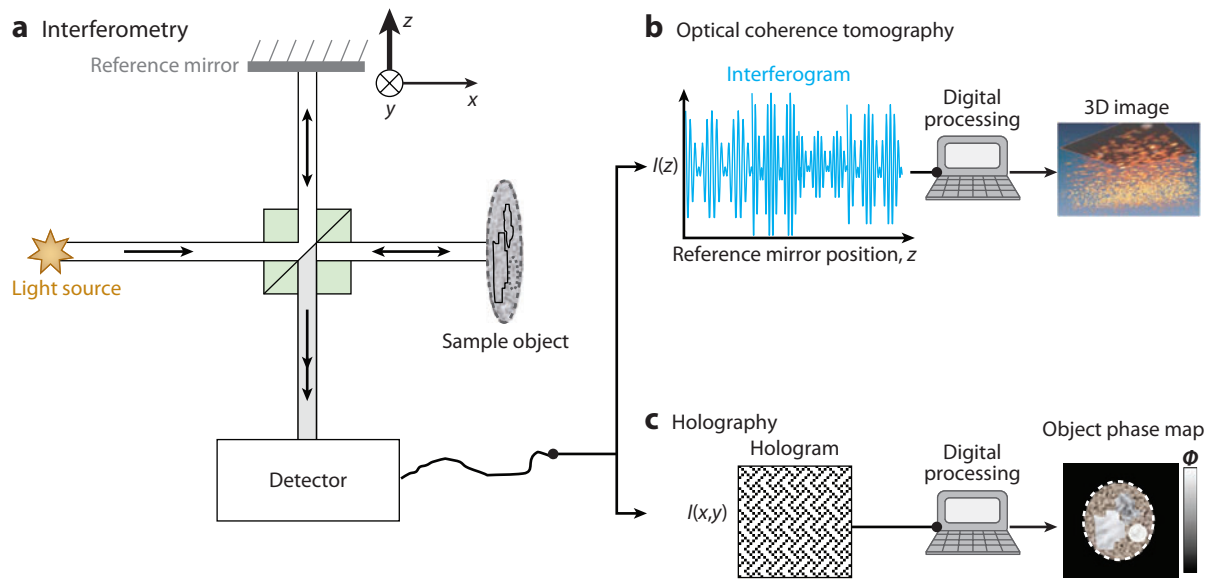
a Interferometry

b Optical coherence tomography

c Holography

Figure 3

(*a*) Phase-sensitive light scattering measurements collected in an interferometer. (*b*) Low-coherence interferometry utilizing a broadband source can be used to collect depth-resolved reflectance data $I(z)$, which can be processed to obtain three-dimensional images of the sample (optical coherence tomography). (*c*) Holograms of the sample object, $I(x, y)$, can be collected and digitally processed to obtain quantitative phase images.

Rayleigh scattering dipoles and often too small to allow geometrical optics approximations of light propagation through them. Elastic scattering by these biological compartments must therefore be described through other theoretical formalisms.

When light interacts with biological tissue, elastic scattering is inevitable. Any spatial variation in refractive index leads to light scattering. The tissue structure and the spatial distribution of refractive index are interlinked. A simple relationship expresses the optical refractive index n through the local molecular density: $n = n_0 + \alpha\rho$. In this equation, n_0 is the refractive index of the medium surrounding a particular scattering structure, α is the specific refraction increment, and ρ is the local concentration of solids (mostly macromolecules such as DNA, RNA, proteins, and lipids). As far back as the 1950s, it has been shown that the majority of substances found in living cells have approximately the same $\alpha \sim 0.18$ (5). This implies that a particle composed of 100% protein would have a refractive index that is 0.18 higher than that of water. Despite its apparent simplicity, this linear relationship was shown to hold for ρ at least up to 50%, thus covering the entire physiological range. Remarkably, the value of α does not significantly vary for different types of macromolecules. Thus optical refractive index is a measure of local density and, as such, tissue architecture. This underlines the power of light scattering as a tool in probing tissue architecture.

If the information about the spatial distribution of mass density in cells and tissue were known, one could explicitly relate light scattering observables—such as the distribution of intensity over angle and spectrum, or the phase of scattered light—to the underlying tissue structure, at least in principle. The problem is that little is known about the spatial distribution of macromolecular density inside cells and tissues. In fact, this is one of the reasons behind interest in light-scattering-based microscopic techniques such as those discussed in Section 7 (6–9).

A central question is how to treat the origin of scattering. Perhaps the most popular approach is the approximation of isolated scattering particles. In the simplest form of this approximation, Mie theory, which describes scattering by homogeneous spheres of arbitrary size and refractive index, is used. In particular, Mie theory has been used to determine size distributions of tissue scatterers based on angular or spectral scattering patterns. A criticism of this approach is twofold: First, tissue is not composed of spherical particles; second, Mie theory is valid only for isolated scatterers—i.e., scatterers would have to be in the far field of one another. Generally, none of these conditions are satisfied in tissue. On the other hand, recent studies show that Mie theory–based interpretation of light scattering may indeed help elucidate (at least qualitatively) the distribution of length scales of spatial refractive index variations (rather than the distribution of real scattering particles) (8, 10, 11).

The limitation of Mie theory with respect to its inability to treat nonspherical and heterogeneous particles can be lifted through the use of approximations to the integral equation of light scattering: the Wentzel-Kramers-Brillouin (WKB) approximation (also known as the van de Hulst or the anomalous diffraction approximation—valid for optically soft particles much larger than the wavelength of light, such as cells and cell nuclei) and the Born approximation (valid for micron-size and submicron particles, such as small organelles) (10, 12–15). In particular, the total scattering cross section of a heterogeneous, nonspherical particle is similar to that of the equiphase sphere (EPS), i.e., a sphere that would produce the same maximal phase shift as the particle. The EPS approximation works best for particles with fine grains of either refractive index or surface perturbation (11). A combination model that utilizes the Born and the WKB approximations has recently been developed (15).

The second major limitation of the Mie theory (isolated particle scattering) can be addressed by the consideration of tissue as a random continuum of spatial refractive index variations. A comprehensive approach to describe tissue microarchitecture is through the mass-density spatial correlation function, which is linearly proportional to the refractive-index correlation function $C(r)$. Typically, the spectral and angle-dependent properties of light scattering are sensitive to $C(r)$ for length scales r from ∼λ/20 (∼20 nm) to a few microns. Light scattering observables are then expressed in terms of the properties of $C(r)$. In a particular case of randomly homogeneous, isotropic correlation with no internal boundaries, researchers developed a three-parameter model based on the Whittle-Matérn functional family to describe some of the most popular types of the correlation (16, 17). This $C(r)$ is defined by index m that defines its shape, the average amplitude, and the length scale of the spatial variations of refractive index. If $m < 1.5$, $C(r)$ is a mass-fractal correlation with the mass-fractal dimension $D = 2m$; if $1.5 < m < 2$, $C(r)$ is a stretched exponential; if $m = 2$, it is an exponential function; finally, $m \gg 1$ corresponds to the Gaussian correlation. The key optical properties that can be measured in elastic scattering studies (e.g., reduced scattering coefficient μ'_s and anisotropy factor g) can then be expressed through these three parameters. In particular, it was shown that the spectrum of the reduced scattering coefficient (frequently measured in light scattering experiments) depends primarily on the value of index m: $\mu'_s \propto \lambda^{2m-4}$ (for $m < 2$). Many scattering techniques can measure $\mu'_s(\lambda)$ and thus can be used to determine the type of the refractive-index correlation function simply by determining the power law of its wavelength dependency.

An even more rigorous solution would require taking into account the heterogeneous distribution of refractive index, including length scales as small as a few nanometers and as large as tens of microns, without making the assumptions of the random isotropy and the absence of internal boundaries. This is currently beyond analytical realm, and computational methodologies must be used: The only means to accomplish this is by numerically solving Maxwell's equations. Recently, new powerful numerical approaches such as finite-difference time-domain (FDTD) and

pseudospectral time-domain (PSTD) computations have become available. Although the use of these computational methods is currently limited by computer resources, we should expect the development of a more robust understanding of tissue scattering as more powerful computers are made available in the future.

4. ADVANTAGES OF UTILIZING LIGHT SCATTERING FOR SENSING

As in any optical sensing application, the performance of sensing methodologies based on elastic scattering interactions of light with biological tissue can be assessed based on four basic parameters: speed of detection, sensitivity, spatial resolution, and specificity. Owing to the large cross sections of the elastic light scattering process, optical scatter signal throughput is typically much higher than signals originating from other light-tissue interactions under similar acquisition conditions consisting of the same collection optics, illumination power, and photodetector sensitivity. For example, to achieve a desired signal-to-noise ratio, a wide-field microscopic image of a cell acquired in phase-contrast microscopy—in which contrast is based on elastic light scattering interaction— can be acquired approximately two orders of magnitude faster than a fluorescence image of the same cell in which an exogenous, high-efficiency fluorophore is used to label a specific biochemical entity.

The spatial resolution of current optical scatter imaging methods is limited by diffraction. Methods such as confocal reflectance microscopy or various phase-contrast methods usually afford lateral spatial resolution on the order of $\lambda/2NA$, where λ is the wavelength of the light and NA is the numerical aperture of the imaging optics. Axial resolution is on the order of 0.5 μm in confocal reflectance microscopy of tissue (18), a few microns in optical coherence tomography (19), and 0.5–1 μm in holographic interferometry (20). Image resolution based on contrast from elastic scattering is governed by principles that apply without the requirement for fluorescence emission or nonlinear fluorescent probes. Thus super-resolution approaches such as synthetic aperture methods (see also Section 8.2) and structured illumination could in principle be applied to imaging field intensities, such as reflectance, formed by scattered light (21).

Whereas image resolution may be limited by diffraction, optical elastic scattering signals remain highly sensitive to changes in the physical properties of the scattering sources that are below the diffraction limit. Thus changes in the dimensions of the scattering sources on the order of tens of nanometers can be achieved through optical scatter measurements (22). Changes in optical path length on the order of nanometers (23) and refractive index fluctuation on nanometer length scales (9) have also been reported within cells.

Based on this discussion, it is clear that sensing based on optical scatter contrast provides superior signal throughput compared with other contrast modalities, affords high sensitivity to changes in object structure, and provides high imaging resolution without relying on exogenous markers. However, one important attribute of bioimaging techniques is molecular and functional specificity. In this regard, optical scatter spectroscopy and imaging of unstained biological tissue is nonspecific. This nonspecificity is twofold. First, elastic scattering provides data about the structure of the biological scatterers. Thus unlike fluorescence, which provides chemically specific data, elastic scattering data are inherently structurally specific but not molecularly specific. Second, the structural data measured by light scattering may originate from multiple scattering sources within a given resolution element and does not a priori necessarily correspond to a specific biological source. By analogy with fluorescence microscopy, a recent thrust has been directed at designing optical scatter molecular probes whose scattering (rather than fluorescence) properties can be used in imaging methods based on elastic scattering contrast. These probes, which are discussed

in Section 9.1, can be used to enhance the signal of specific molecular targets and thus confer specificity onto the optical scatter signals.

Different experimental approaches have also been used to correlate light scatter measurements with molecular or biological function in unlabeled or fluorescently labeled samples (see Section 5). However, optical scatter data that are not molecularly specific can still be valuable. This is especially true for optical scatter imaging modalities (e.g., reflectance confocal microscopy and optical coherence tomography; see Section 7), which can be used noninvasively in vivo for microscopic visualization of tissue structure safely, at low cost, and without the use of exogenous dyes. In addition, light scattering measurements can provide a means to track noninvasively biophysical changes within tissues and cells. Although such changes may not be molecularly specific, they still result from a combination of biological functions that affect structure. Thus these biophysical changes can be used to search for tissue alterations in cases when a priori knowledge of the molecular pathways involved does not exist or when such knowledge is difficult or too costly to obtain. In these cases, the light scattering measurements can be used as an initial screening tool to identify time points during treatment or tissue regions that exhibit significant changes in optical scatter signal compared with an established baseline. Further biochemical analysis can then be guided to these specific time points or regions. This screening is noninvasive and can be accomplished rapidly with minimal sample preparation or processing.

5. BIOLOGICAL INTERPRETATION OF THE OPTICAL SCATTER DATA IN UNLABELED OR FLUORESCENTLY LABELED SAMPLES

Optical scatter data collected from unlabeled biological tissue provide structural information that can originate from different biological compartments and interfaces, including tissue boundaries, cells, organelles, or macromolecular complexes. Because multiple genes, proteins, or organelles can contribute to changing the observed scattering variables or spatial patterns, the difficulty in interpreting changes in light scattering signals from a molecular biology standpoint remains. There are several potential sources that can underlie the biophysical structural variables measured by light scattering, and the specific direct relationship between each of these biological sources and the scattering measurement is not always known a priori. We discuss several approaches that have been used for correlating optical scatter measurements with molecular and biological processes.

5.1. Isolating the Scattering Structure

Studying the scattering properties of individual biological structures can be achieved by physically isolating a structure of interest. This is best illustrated by the well-known light scattering studies of isolated viable mitochondria that were used to understand the relationship between mitochondrial function and mitochondrial matrix structure under different bioenergetic conditions (24–30).

On the other hand, structural information can be obtained noninvasively in an imaging regime in which light scattering interactions are utilized to directly visualize the scattering particles. In this case, the scattering sources can be spatially isolated in the image, and their structure can be determined within the resolution of the optical system. Identifying a specific scatterer within an image requires that the scattering signature and spatial pattern be specifically representative of the desired structure while excluding other structures as potential contributing sources. Large biological structures with specific morphologies, such as cells and nuclei, are easily identified with these methods. However, when probing subcellular compartments, quantitative optical scatter imaging methods still do not provide the specificity needed to identify directly specific organelles

and subcellular structures in unlabeled cells. For this, additional modalities can be used to confer
biological specificity.

5.2. Multimodal Imaging

The structural data provided by the biophysical light scattering interaction of light with tissue
can be combined with biochemically specific measurements to study processes that occur at the
organellar or molecular levels. This can be achieved in unlabeled tissue through the combination
of elastic scattering data with autofluorescence (31) or Raman (32) signals. Multimodal data can
also be obtained through the combination of the elastic scatter measurements with signal from
fluorescently labeled tissue (33–36). This allows correlation of the optical scatter data with molec-
ular components that do not normally autofluoresce and provides more flexibility in interrogating
desired molecular pathways.

Although the spectroscopic elastic scattering data may be found to correlate with changes
in the biochemical signals, the elastic scattering data may not necessarily originate from the
same specific biological source unless the optical scatter and biochemical signals can be spatially
registered. In principle, this can be achieved through multimodal imaging, in which the same
biological source can be spatially isolated and interrogated by different imaging modalities such
as light-scattering-based optical coherence tomography and two-photon fluorescence microscopy
(37, 38). The specificity of the scatter signal in multimodal approaches therefore requires that
the scattering signal within a given resolution element be dominated by scattering by a single
biological source, and that this specific biological source be positively identified by a biologically
specific modality such as fluorescence.

5.3. Biological Specificity Acquired by Training Data

Light scattering information can be utilized to differentiate and classify a finite set of samples
comprising different, but well-defined (e.g., normal, dysplastic), groups of unlabeled cells or tis-
sues with great sensitivity and specificity. Multimodal approaches are also valuable in this con-
text by providing multiparametric data that can improve diagnosis and tissue classification (39).
However, the specificity of the light scattering measurements made in these classification con-
texts is "constrained" to the extent that it is still limited to the context in which the experiments
are undertaken. In particular, it is not clear whether the same positive scattering changes will
always be unequivocally indicative of the biological transformations under study, or whether
other physiological states can result in similar effects in a set of unknown samples. In cell biol-
ogy experiments, researchers can address specificity by demonstrating that the measured positive
scattering signal can be modulated or blocked by molecular or biochemical experimental treat-
ments that affect a specific signaling pathway. Nonetheless, in cases when biochemical modulation
of the scatter signal is not possible, such as in signals collected in vivo from patients, extensive
validation studies are required to exclude unrelated processes that could potentially give rise to
the same scattering changes. To this end, some investigators have begun to address this issue by
testing sample conditions that fall outside the initially sought class definitions (negative controls).
For cancer diagnosis, conditions such as age, gender, race, demographic factors, or smoking his-
tory that could confound the light scattering data were, for example, considered and ruled out
(40). With adequate and sufficient training data, this approach could ultimately lead to the ability
to screen for specific biological conditions in unknown tissue samples. Although these optical
scatter classification studies do not currently provide a comprehensive data set encompassing all
possible cellular and tissue states, these studies are still valuable in providing the positive scattering

responses of biological conditions such as cancer. As noted above, these positive responses can be used as an initial screen to identify the presence of biological change within a given sample and to guide further tissue analysis.

6. LIGHT SCATTER SPECTROSCOPY TO ASSESS TISSUES IN VIVO

Imaging and spectroscopic light scattering techniques have the potential to complement current diagnostic tools. Elastic scattering can be performed in vivo, and the obtained information is quantitative. Furthermore, researchers can potentially obtain information about cell organization at length scales as small as a few tens of nanometers (8, 9, 11). Visualization of such small objects with far-field optical microscopy is difficult or impossible because the required resolution is below the diffraction limit. Spectroscopic analysis of light scattering, on the other hand, enables obtaining such information because it does not attempt to *visualize* these small objects. Whereas the resolution of a light microscope is limited to $\sim\lambda/2$, with $\lambda \sim 400$–700 nm being the wavelength of light, characteristic spectral features of light scattered by particles as small as $\lambda/20$ can be distinguished (8, 11, 13, 14).

Most biomedical applications of light scattering rely either on light transport in macroscopic tissue (e.g., elastic scattering spectroscopy) or light interaction with localized microscopic volumes of biological media (e.g., light scattering microscopy modalities). From the perspective of "macroscopic" applications, light scattering has been employed to obtain insights into tissue structure. A common strategy (pursued either explicitly or inexplicitly) is to measure the distribution of light scattering intensity as a function of either wavelength or the scattering angle (**Figure 4**), translate these measures into specific optical properties of tissue, and finally, link these optical parameters to the tissue structural properties. This last step is dependent upon the availability of the robust models of light scattering in tissue that enable solving the inverse scattering problem. Although the origin of light scattering in tissue has not been fully elucidated, substantial progress has recently been achieved (see Section 3). Some of the key optical properties that can be measured are the
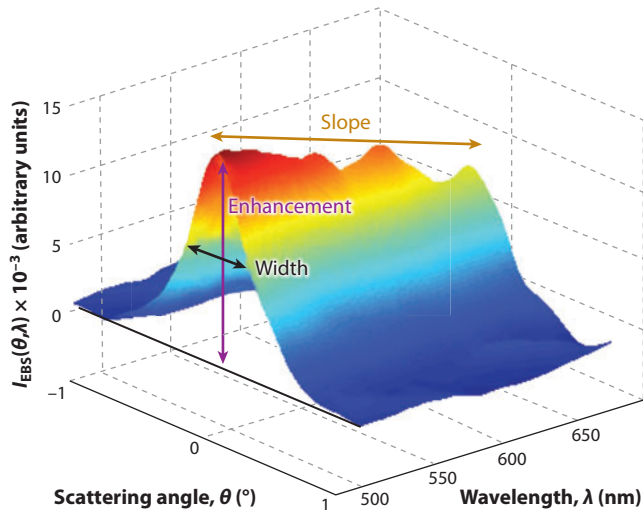

Figure 4

Low-coherence enhanced backscattering (LEBS) recorded from human colonic mucosa as a function of angle and wavelength.

reduced scattering coefficient μ'_s (i.e., the total scattering cross section per unit volume) and the characteristics of the scattering phase function (such as the anisotropy factor g, the relative portion of side scattering, the backscattering cross section, or the phase function for a given angular range).

Elastic scattering spectroscopy was used for tissue diagnosis and showed clear differences among healthy and precancerous colonic tissues (41, 42). Diffuse optical tomography (DOT) to measure scattering properties of tissue (μ'_s in particular) showed that it can be used as a marker of malignancy (43–48). The angular and spectral properties of scattered light were measured by low-coherence interferometry to quantify one of the most ubiquitous markers of neoplasia: increased cell nuclear size (36, 49, 50). Light scattering methods were developed to monitor changes in mitochondria and lysosomes in response to photodynamic therapy (35, 51–53) and to investigate changes in mitochondria within cancer cells (54). The size distributions of cellular organelles in live cells were also measured with light scattering to distinguish different types of immune cells (55). A multimodal study utilizing light scattering and autofluorescence showed alterations in subcellular organization yielding larger and less organized subcellular membrane units that were accompanied by a more diffuse subcellular distribution of tryptophan. This study also showed a decreased redox ratio in normal keratinocytes compared with their human papillomavirus-transformed counterparts (31). Polarized light scattering spectroscopy was utilized to quantify the fractal properties of bioengineered tissue (56). Low-coherence enhanced backscattering (LEBS) was developed to measure depth-resolved optical properties of tissue (μ'_s, g, and the index of the refractive-index correlation function m; see Section 3 for details) (57–60).

Enhanced backscattering originates from the constructive interference of photons traveling time-reversed paths in a scattering medium. This results in a peak of scattered intensity centered around the backscattering direction (**Figure 4**). The width of this peak is proportional to $\lambda\mu'_s$, which, in weakly scattering media such as biological tissue, is extremely small ($\sim$0.001°). The difficulty involved in resolving these sharp peaks can be avoided by the recording of enhanced backscattering under low spatially coherent illumination (the spatial coherence length $Lsc \ll 1/\mu'_s$), which broadens the peak by as much as two orders of magnitude (57–61). Low spatial coherence serves as a spatial filter that effectively limits the area of light collection to $\sim Lsc^2$, and the LEBS signal primarily results from the interference of short traveling photons that emerge from the point of entry into the tissue at distances less than Lsc. This feature enables researchers to achieve depth-resolved assessment of tissue by analyzing the angular profile of a LEBS peak, by analyzing its Fourier transform that contains information about a range of tissue depths, or by selecting Lsc to target a desired depth. For a given Lsc, the most probable penetration depth is $\propto Lsc^{2/3}/\mu'^{1/3}_S$. The angular profile of LEBS depends on the tissue microarchitecture through the refractive-index correlation function $C(r)$. For instance, in the three-parametric approximation for $C(r)$, $C(r)$ can be experimentally characterized if three LEBS parameters are measured, such as its amplitude (the enhancement factor), its peak width, and the power of the spectral dependency of the enhancement factor (the latter is proportional to the spectral slope shown in **Figure 4**), with all these measurements being depth selective. Applications of LEBS demonstrated that alterations in tissue microarchitecture are a ubiquitous phenomenon that develops in the earliest stage of carcinogenesis in a number of cancer types (62, 63). This is just one of many examples of how new light scattering techniques can lead to new frontiers in biology.

7. IMAGING BASED ON OPTICAL SCATTER CONTRAST

Several well-known microscopic visualization techniques derive contrast from optical scatter interactions with biological tissue. These include Zernike phase contrast, differential interference contrast, and dark-field microscopy. These methods enable the visualization of nonabsorbing

biological specimens based on spatial variations in optical phase across the sample. Thus one of the main advantages of optical scatter contrast is that it can be used noninvasively to image unlabeled tissue. This is especially relevant in clinical applications in which the rapid, safe, and low-cost assessment of unstained tissue in vivo is highly desirable. However, to enable imaging of thick tissues in vivo, an important requirement is that the optical instrumentation allows viewing individual tissue planes with sufficient axial resolution as a function of tissue depth. We describe two methods that rely on different optical principles to achieve noninvasive "optical sectioning" and three-dimensional imaging in vivo. The first method utilizes confocal microscopy principles to reject out-of-focus light. The second utilizes temporal coherence gating. The image signal in both methods is given by the local reflectance of the tissue. Both methods ultimately produce a spatial tissue map depicting tissue architecture and the spatial distribution of the different scattering tissue structures. Owing to their optical sectioning ability and out-of-focus background rejection, these imaging modalities provide tissue images in vivo with microscopic-scale resolution.

In addition, methods that combine light scattering spectroscopy with microscopy as well as quantitative phase imaging methods have been developed to extract the local optical properties of a microscopic biological sample. Rather than focus solely on sample visualization, these methods aim to create images that directly encode quantitative light scattering data. The value of each pixel in these encoded images can provide direct information about the local scattering sources' size, shape, and refractive index.

7.1. In Vivo Confocal Reflectance Microscopy

Since the 1990s, confocal microscopy (64) has become a widely used method for in vitro biological imaging with commercially available bench-top instruments. Scanning confocal microscopy is typically used for fluorescence imaging in biological applications. However, the method can also be applied to reject out-of-focus light and to create optical sections in a backscattering reflectance regime in systems that allow partial transmission and reflection of the light to and from the sample at the same wavelength. Because fluorescent dyes cannot always be used in vivo, clinical imaging based on confocal reflectance microscopy can provide a powerful, noninvasive method to visualize tissue structure for diagnostic purposes, and portable clinical systems are now available (e.g., confocal imagers from Lucid, Inc.). Typically, these systems employ an epi-illumination configuration with high NA objectives. The lateral resolution of the system is set by the NA of the objective used, whereas the axial resolution is determined by the size of an adjustable detector pinhole similar to that in a bench-top confocal microscope (65). In highly scattering tissues, such as skin, resolutions of 0.5–1 µm laterally were achieved at 350-µm depth at near-infrared wavelengths (18). Instrumental optical sectioning is 1–2 µm. However, this sectioning ability can degrade to 3–5 µm due to the effects of scattering and aberrations. Sources of aberrations in skin are the distribution of melanin and keratin in the epidermis, the layered nature of cells, and the highly corrugated dermo-epidermal junction (M. Rajadhyaksha, personal communication). A recent research thrust in this area has been the miniaturization of confocal microscopes for in vivo applications. Simplified scanning methods such as line scanning are being investigated to this end, and they can greatly simplify microscope design without significantly compromising resolution (66). Fiberoptics-based reflectance confocal microscopes for "endomicroscopy" are also a significant thrust (67).

A spectroscopic extension of confocal reflectance microscopy was recently developed to collect, at each scanned point, a scattering spectrum that is processed to yield a measure of local particle size or shape at each voxel (68). The scattering spectrum is obtained through the illumination of the sample with a focused broadband spot. Passing the light scattered by the sample into a spectrometer retrieves a scattering spectrum of the particles contained within the analyzed spot.

A model fit to the spectroscopic data that utilizes either Mie theory (3) or the T-matrix method (69) retrieves the size, aspect ratio, and refractive index of the sample at each scanned location. This method, confocal light absorption and scattering spectroscopy (CLASS), was demonstrated by measuring alterations in the size of organelles within living cells treated with docosahexaenoic acid (8).

7.2. Optical Coherence Tomography and Microscopy

Optical coherence tomography (OCT) is a biomedical imaging modality that is increasingly being used for clinical imaging, primarily in the areas of ophthalmology, cardiology, dermatology, and oncology (70–73). OCT performs imaging by interferometrically detecting singly backscattered light to render a depth-resolved image of biological tissues. Most commonly, OCT utilizes fairly low-NA optics when focusing light into specimens, so as to have a long confocal parameter that approximates the depth at which OCT can image in highly scattering tissue (typically <2 mm), thereby maintaining a relatively uniform transverse resolution throughout the imaging depth. This long confocal parameter, however, comes at the expense of lower transverse resolution. Optical coherence microscopy (OCM) (37, 74) similarly utilizes interferometric detection, but with higher NA optics to capture *en face* optical sections at various depths, as performed in reflectance confocal microscopy or most all other high-resolution optical microscopic imaging techniques. The combined use of confocal-gated optical sectioning with coherence-gated optical ranging permits OCM to depths in highly scattering tissues that can exceed those of standard reflectance confocal microscopy (74).

Spectroscopic OCT or OCM (SOCT/SOCM) was developed out of OCT/OCM to take advantage of the broad spectroscopic content of the light used in these techniques (75–77). The SOCT technique enables spectroscopic analysis on the backscattered signals to extract information about the scatterers and absorbers in tissue, providing new metrics for functional and molecular imaging. Advances in SOCT/SOCM have enabled discrimination of endogenous tissues and cell types, as well as the detection of exogenous contrast agents (37, 78, 79). A full theoretical and applied description of SOCT/SOCM can be found in an earlier review (76), but the SOCT principles and the duality between time-domain SOCT and frequency-domain SOCT are illustrated in **Figure 5**.

Optical systems that utilize low NA and/or spatially incoherent beams, such as those used in some light scattering spectroscopy (LSS) techniques, generally average the spectroscopic response of the sample over a large number of scatterers. OCT, however, commonly involves moderate focusing, which results in a small number of scatterers contributing to the response. OCM, with high NA optics and tightly focused beams, enables one to resolve individual scatterers, but the analysis of the backscattering response is complicated by the large angular extent of the beam delivery and collection (80). A demonstration of SOCT-based scatterer sizing was performed on tissue phantoms containing known sizes of microspheres (76). Qualitatively, there was good agreement between the SOCT-recovered spectra and predictions based on the vector Mie theory. Most important, the apparent modulation frequency (or pitch) of the spectra, which is directly proportional to scatterer size, was well matched with theory.

The ability of spectroscopic OCT/OCM analysis for analyzing scattering particle size can be extended to tissue specimens and even to individual cells (37, 76). Through the use of a spectral-domain OCM system, spectroscopic OCM was performed on a tissue specimen consisting of regions of adipose and muscle tissue (**Figure 5b**). In this example, two different SOCM analysis methods were performed. The first method was based on metameric imaging, in which the scattering spectrum with the full width at half maximum (FWHM) of the source spectrum was divided

CLASS: confocal light absorption and scattering spectroscopy

OCT: optical coherence tomography

OCM: optical coherence microscopy

SOCT: spectroscopic optical coherence tomography

SOCM: spectroscopic optical coherence microscopy
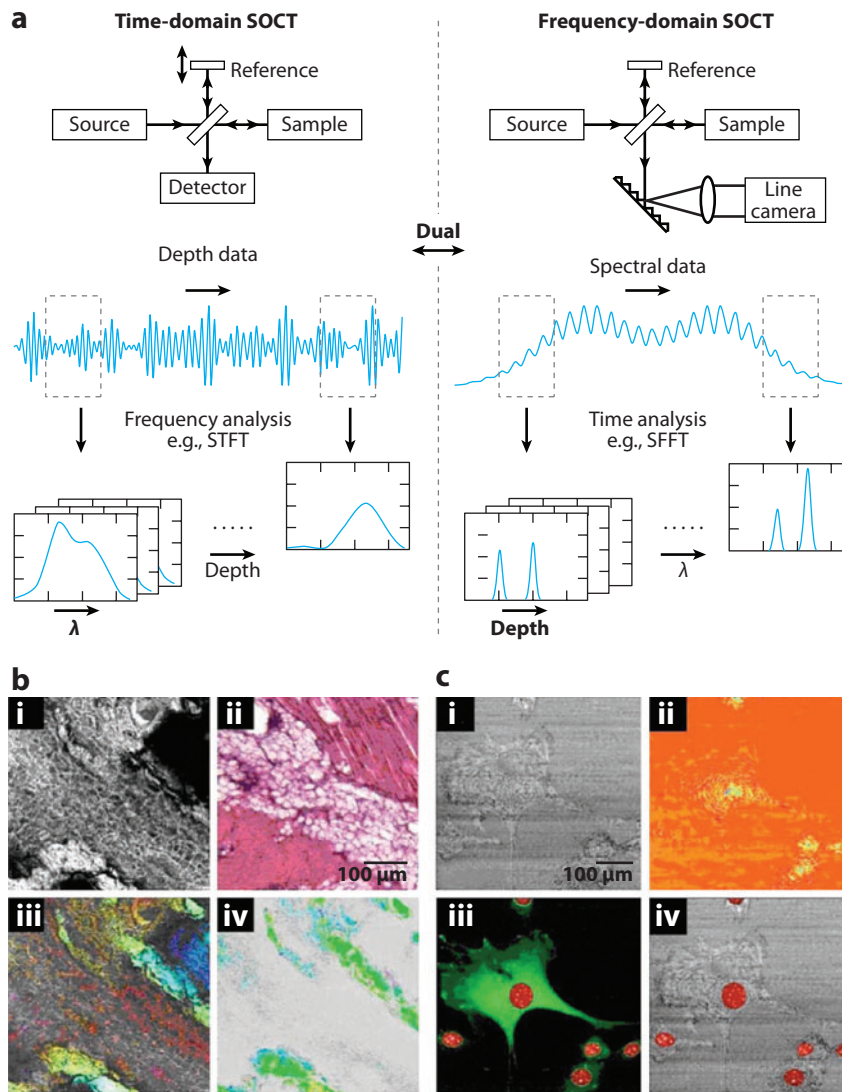
LSS: light scattering spectroscopy

Figure 5

Spectroscopic optical coherence tomography (SOCT) imaging using time-domain and frequency-domain interferometry. (*a*) Short-time Fourier transforms (STFT) and short-frequency Fourier transforms (SFFT) are performed on the acquired OCT interferograms to create 2D spectroscopic optical coherence tomography (SOCT) signals that are indexed by wavelength and depth in the sample or specimen. (*b*) Spectroscopic spectral-domain optical coherence microscopy (OCM). (*i*) OCM of rat tissue containing regions of adipose cells (*middle*) and muscle fibers (*upper right, lower left*). (*ii*) Corresponding histology. (*iii*) Spectroscopic optical coherence microscopy (SOCM) image using metameric spectral analysis. (*iv*) SOCM image using light scattering spectroscopy (LSS) spectral analysis. The scale bar is representative of all images (*i–iv*). (*c*) Single-cell imaging with SOCM. (*i*) Spectral-domain OCM of green fluorescent protein (GFP)-vinculin transfected fibroblasts in culture. (*ii*) Corresponding SOCM image showing localized regions of strong spectral scattering (*yellow-green*). (*iii*) Multiphoton microscopy of GFP fibroblasts co-labeled with DNA-nuclear dye. (*iv*) Overlay of multiphoton DNA-dye fluorescence and OCM images. Comparisons between panels *ii* and *iv* show validation of SOCM spectral analysis for identifying dominant scatterers. Adapted from References 37 and 76.

into three equally spaced subbands, and in which the intensity from the low-, mid-, and high-frequency bands were assigned to the red, green, and blue channels, respectively (**Figure 5b:iii**). This method was found to represent the spectral information similarly to the way that the traditional spectral centroid method does, in which shifts in the spectral centroid are mapped onto colors in the image. This metameric method was found to be more robust and more similar to the processing in human vision. The second method was based on spectral analysis initially proposed in LSS (81). The backscattered spectra are first analyzed by the fast Fourier transform (FFT), and the first peak of the FFT data is used for hue information in a hue-saturation-value (HSV) color scale (**Figure 5b:iv**). This peak position is related to the physical size and interscatterer distance of the dominant scatterers, such as nuclei. These two SOCM spectral analysis methods are only representative of many that can be developed. They do, however, provide examples of how the spectroscopic analysis of scattered light can be used to provide and enhance contrast in optical images in physically meaningful and quantitative ways.

As nuclei are known to be dominant scatterers within cells and tissues, SOCM was used to image fibroblasts in culture to demonstrate the use of these spectral analysis methods at the cellular and subcellular level. Researchers used a novel custom integrated microscope that enables simultaneous acquisition and registration of data from OCM and multiphoton microscopy techniques (37, 82). The OCM images provide information on the tissue and cell structures based on optical scattering, whereas the multiphoton microscopy images provide information on the function, related either by the autofluorescence from the metabolic processes or by functionally labeled, genetically expressed fluorescent proteins [i.e., green fluorescent protein (GFP) coexpressed with vinculin, a cell-surface adhesion protein] (83). **Figure 5c** shows images captured with this system, including SOCM images generated using the LSS spectral analysis method. The transfected fibroblasts expressed GFP-labeled vinculin and were colabeled with a DNA-specific dye (Hoechst 33342) for localization of nuclei relative to the surrounding cell structures. The simultaneous multimodality imaging afforded by this microscope provided overlays of various image channels, as well as the colocalization of the dye-labeled nuclei and the SOCM-identified dominant scatterers within the cell culture.

SOCM analysis with tight focal gating serves to decouple the inherent trade-off between spectral and spatial (depth) resolution. This enables more precise extraction of spectral changes and signatures that can be used to characterize the wavelength-dependent scattering properties of cells and tissues. Wavelength-dependent scattering and the resulting spectral modulation are information-rich processes that can be readily used to extract quantitative information about scatterer size and spacing, as well as to provide novel contrast mechanisms in images. These OCT-based methods offer advantages over reflectance confocal microscopy by enabling deeper imaging penetration into highly scattering tissues, owing to the added coherence gating and the ability to perform depth-resolved spectral analysis to enhance the information content of the images.

7.3. Optical Scatter Imaging Based on Fourier Filtering

Collecting far-field angular scatter data by analyzing the optical transform of biological specimens dates back several decades (84). The far-field angular scattering data can be imaged directly and was recently utilized for automated differentiation of bacterial colonies (85). The scatter intensity pattern can also be collected in a conjugate Fourier plane (transform plane) of a microscope system to extract the angular scattering properties of the scattering sources in the field of view (86). A recent multimodal microscopic design permits imaging the sample's transform in combination with bright-field, dark-field, and fluorescence imaging as well as collecting a wavelength-dependent light scattering spectrum of the sample (52). In the transform plane of a microscopic imaging

system, the scattering intensity is mapped as a function of the polar scattering angle θ with respect to the incident light and of the azimuthal angle φ as alluded to in **Figure 2** (Optical Fourier processing inset). For weakly scattering objects, the angular scatter directions mapped to positions (θ, φ) in the transform plane correspond to the object's spatial frequencies $(U, V) = (\kappa \sin \theta, \kappa \sin \varphi)$, where $\kappa = n/\lambda$ and n is the refractive index of the propagation medium (21).

Unless the incident light is directed to a specific location within the sample, the scattered light measured in the transform plane of the microscope corresponds to scattering by all the scattering sources within the field of view. However, by collecting Fourier-filtered images that are formed by allowing only specific angles of scatter to pass, researchers can remap the angular scatter information in the imaging plane. In this case, multiple Fourier-filtered images are analyzed to extract the sample's angular scattering properties at each pixel within the full field of view. This method was first implemented using two circular Fourier filters designed to measure the intensity ratio of wide to narrow angle scatter. This ratio was shown to decrease monotonically with particle size (6) and was shown to track dynamic cellular changes during calcium injury (87) and apoptosis (33). The scatter changes were modulated by biochemical and genetic modifications affecting mitochondria (34, 87). Recent implementation of a digital micromirror device as a Fourier filter allows filtering any desired combination of scattering angles (or spatial frequencies) within the NA of the microscope (88). The method was demonstrated using tunable Gabor-like spatial filters with Gaussian envelopes, which provide signal localization in both Fourier and image space (89). The Gabor filtering method is sensitive to differences in particle size on the order of 30–50 nm (90) and to changes in particle orientation and aspect ratio (88). Alterations in organelle aspect ratio were measured in isogenic, Bax/Bak-expressing, apoptosis-competent cells (W2) and Bax/Bak-null, apoptosis-defective cells (D3) (7). As expected, the Bax/Bak null cells, which are expected to be deficient for mitochondrial fusion and have shorter mitochondria (91), also had a larger number of particles with a lower mean aspect ratio as measured by the optical Gabor filtering method (**Figure 6**).

Although based on elastic scattering contrast, the Gabor filter–based technique does not rely on a detailed inverse scattering model or on Mie theory to extract morphometric measurements (90). This technique is therefore applicable to nonspherical organelles for which a precise theoretical scatter description is not easily given, and it provides distinctive morphometric parameters that can be obtained within unstained living cells to assess their function. The technique is advantageous compared with digital image processing in that it operates directly on the object's field transform rather than the discretized image of the object. Thus it does not rely on high image-sampling rates. High sensitivity at low resolution was demonstrated using aliased images of microspheres (90). The cell data are also shown after block-processing the initial Gabor-filtered images such that every adjacent 4×4 pixel region is averaged into one pixel before orientation processing, effectively demagnifying the filtered images from 512×512 to 128×128 pixels, or approximately $1\ \mu m^2\ pixel^{-1}$ (**Figure 6d,e** and Reference 7). Although the pixels in the resulting images are large, they still demonstrate orientation detection substantially similar to that of the high-magnification images (**Figure 6g**). A real $4\times$ demagnification corresponds to imaging 300–500 cells instead of 20–30 at comparable seeding densities. Thus this method can ultimately be applied to high-throughput, single-cell analysis within relatively large fields of view.

In the applications described here, the sample illumination usually consists of a collimated beam of light aligned with the microscope axis. Collection of scattered light by a microscope objective with a collimated goniometric illumination assembly has also been proposed (92). In contrast, a recent application in which the incident light is focused to a 7-μm spot size was described. Angular elastic scatter data originating from a single cell were collected in a conjugate Fourier plane of the microscopy system, while the scattered light was also analyzed spectrally to
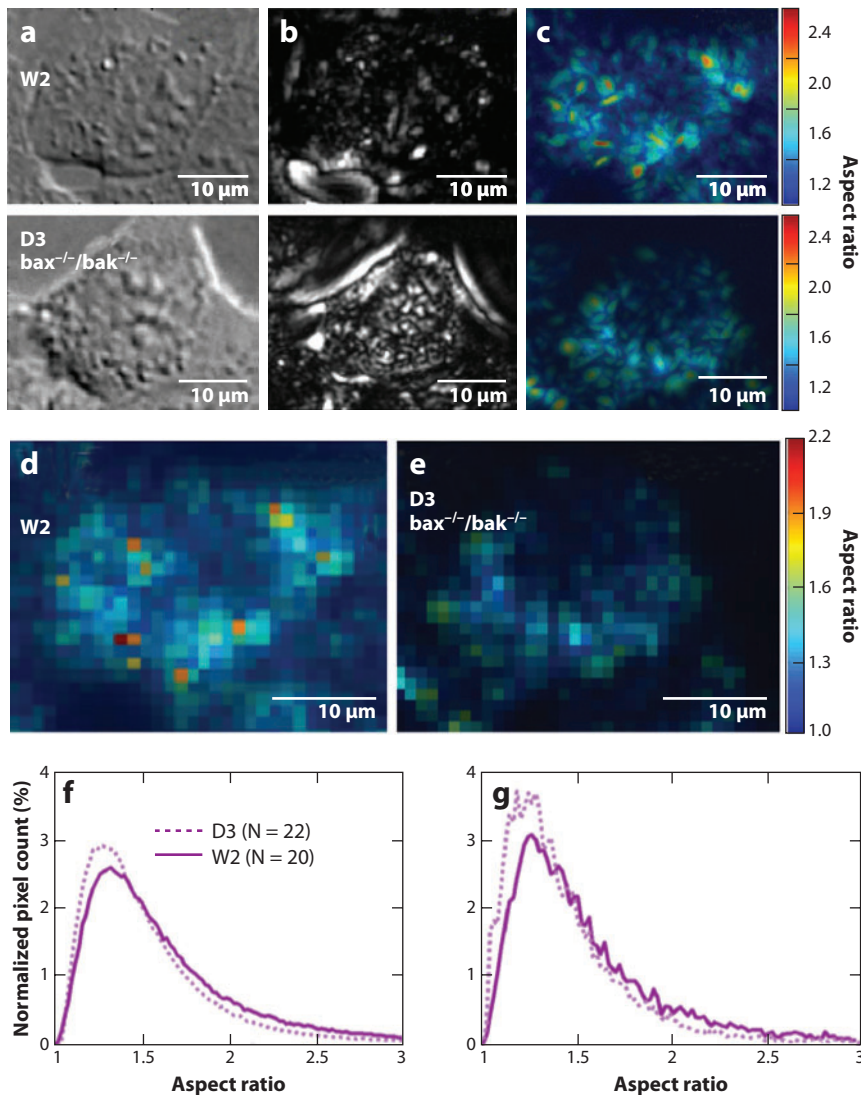
Figure 6

Bax/Bak-expressing (W2) and Bax/Bak-null (D3) cells. (*a*) Differential interference contrast. (*b*) Dark field.
(*c*) Object orientation showing more highly oriented objects (*red areas*) in the W2 cell compared with the D3
cell. (*d*, *e*) W2 and D3 orientation images after block-processing the initial Gabor-filtered images to simulate
a 4× demagnification. Data were collected using an orientation-sensitive Fourier filter bank consisting of
nine Gabor-like filters with period S = 0.95 μm, Gaussian envelope standard deviation σ = S/2 = 0.45 μm,
and orientations φ = 0° to φ = 160° in 20° increments (see also Reference 7). The color intensity in panels *c*,
d, and *e* represents the overall response (sum of all responses) of the pixel to the filter bank; the color hue
encodes the degree of orientation. The degree of orientation was calculated as the ratio of maximum
intensity to the average of all the responses collected as a function of filter orientation and was taken as a
measure of aspect ratio. (*f*, *g*) Pixel histograms of W2 (N = 20) and D3 (N = 22) cells (*f*) before and
(*g*) after pixel binning. In panel *f*, the mean aspect ratio parameter per cell was 1.58 for W2 and 1.38 for D3
(p < 0.04 by student t-test). In panel *g*, the mean aspect ratio parameter per cell was 1.54 for W2 and 1.35
for D3 (p < 0.05 by student t-test). Adapted from Reference 7 with permission.

yield a Raman spectrum of the same cell. Theoretical predictions of angular scatter of a focused beam are used to extract structural information, which is combined with chemical data based on Raman scattering (32). This method has recently been applied to the study of immune cells with the potential for future monitoring of developmental processes in these cells (55), and it provides a basis for analyzing angular backscatter data from samples illuminated by a focused laser beam.

7.4. Quantitative Phase Microscopy

Quantifying the optical phase and scattering properties of the sample is difficult to achieve if the process is based directly on the intensity of images acquired by conventional phase contrast or differential interference contrast methods. Thus interferometric methods based on the principles of holography (93) are used for quantitative phase imaging. With advances in charge-coupled device (CCD) camera design and performance, it was recently shown that holograms with sufficient spatial resolution can be recorded digitally on a CCD camera (94). This allows the digital reconstruction of the object's field amplitude and phase by numerical computation (95). This approach, now widely known as digital holographic microscopy, has gained a significant amount of interest since its inception. For a full review of digital holography methods, the reader is referred to References 96 and 97.

Different interferometric imaging systems and methods for object reconstruction have also been proposed for quantitative phase imaging (98, 99). Interferometric quantitative phase microscopy is especially attractive for biological imaging because it provides highly sensitive and high-resolution quantitative phase maps of nonabsorbing biological samples. The quantitative phase information can be used to study cell function dynamics, subcellular structure, and organelle distribution with high phase and temporal sensitivity (100). In general, quantitative phase microscopy methods provide an integrated measurement of the optical phase throughout the axial thickness of the sample. The refractive index and sample thickness are therefore intertwined within the measurement of the optical path length. However, refractive-index tomographic imaging of cells and tissues has been recently demonstrated (20, 101).

Another innovative approach to extract subcellular refractive-index fluctuations has recently been proposed. Partial wave spectroscopy utilizes measurements of the backscattering spectrum to assess refractive-index fluctuations in epithelial cells (9). In this case, the sample is illuminated by a broadband source and a low NA objective to obtain light scattering spectra at each resolution element. Spectral fluctuations in light scattering are analyzed to extract a measure of refractive-index fluctuations as a function of depth at each subcellular location. Partial wave spectroscopy captures the axial fluctuations in subcellular structure into a single parameter, which gives a measure of disorder strength over a sample depth on the order of several microns. Although the size of the resolution element is determined by the NA and depth of field of the objective, the scattering data reflect structural fluctuations on the order of 10 to 100 nm. Recently, this method was shown to detect reproducibly nanoscale, subcellular structural changes that were associated with genetic changes induced by the field effect of carcinogenesis (40).

Finally, the scattering properties of a biological sample also depend on the polarization of the incident light and birefringence properties of different molecular constituents (102). Quantitative polarization microscopy has been developed to measure retardance and molecular orientation within biological tissues (103). The method provides diffraction-limited microscopic resolution and reports on highly oriented biological structures, such as actin (104), microtubules (105), and collagen (106).

8. COMPUTATIONAL METHODS IN OPTICAL SCATTER IMAGING AND SPECTROSCOPY

Computational methods are essential for quantitative optical scatter imaging and spectroscopy for both modeling and interpreting the light scatter data, as well as for image reconstruction. Two current examples in computational approaches are presented here: (*a*) applications of the FDTD method to infer the scattering properties of biological samples, and (*b*) interferometric synthetic aperture microscopy (ISAM) for improvement of three-dimensional imaging.

8.1. Finite-Difference Time-Domain Methods

To various degrees, the current modeling methods used in tissue optics neglect the full-vector, electromagnetic-wave nature of light, especially with regard to near-field interactions of closely spaced scatterers. Furthermore, recent progress in developing realistic light scattering models to interpret the wealth of information hidden in light scattering data (see Section 3) depends on the ability to validate these models. Although experimental validation remains difficult (this would require knowing the spatial distribution of refractive index in tissue with nanoscale precision), the focus has shifted toward numerical techniques. The most rigorous approach involves solving Maxwell's equations. This can be accomplished through the use of the FDTD method. Originally developed for military applications, FDTD is now finding new applications in tissue optics.

With currently available computers, the FDTD numerical method for solving Maxwell's equations permits straightforward numerical modeling of full-vector, electromagnetic-wave interactions with inhomogeneous material structures spanning approximately 1000 wavelengths or fewer in two dimensions, and 100 wavelengths or fewer in three dimensions. This capability is appropriate for calculating optical interactions (wavelengths $\sim$0.4–1 µm) with structures within biological tissue (characteristic dimensions $\sim$0.001–50 µm). Calculations of interest include the internal optical electric-field standing-wave distribution; the differential (bistatic) scattering cross section; and the total scattering cross section. Early applications of FDTD included modeling of light interaction with retinal cells (107) and phenomenological studies of the role of organelles in light scattering by cells, in which cells were modeled as consisting of randomly distributed, isolated, nonspherical scattering particles (108–111). More recently, FDTD was used to study light scattering in media with spatially continuous refractive-index variations as well as the light scattering behavior of randomly inhomogeneous and nonspherical structures, typical for tissue optics (10, 11, 13, 14, 17, 112, 113).

Although, in principle, FDTD could be used to model light interaction with tissue that spans macroscopic dimensions, this has not been feasible because even the most powerful existing computers lack the capabilities to deal with the enormous database of electromagnetic-field vector components mandated for FDTD. To attack this problem, researchers developed the PSTD numerical algorithm to solve the full-vector Maxwell's equations. PSTD is an innovative variation of FDTD wherein the spatial derivatives in Maxwell's curl operators are implemented using fast Fourier transforms. This yields infinite-order accuracy, i.e., essentially exact results for electromagnetic-field spatial modes sampled according to the Nyquist criterion. That is, the PSTD meshing density can approach two samples per wavelength in each spatial dimension, which is approximately an order-of-magnitude reduction from the meshing density required by FDTD. This yields an enormous decrease of computer resources relative to FDTD and thereby permits using PSTD to directly model realistic three-dimensional tissue regions that have spans as large as hundreds of microns to millimeters. Within such a volume, PSTD can provide the complete near- and

far-field interactions of hundreds, even thousands, of arbitrarily complex biological structures with no simplifications other than the subwavelength discretization of the refractive-index distribution (114–116). In particular, PSTD has been used to model light transport in media with the overall sizes up to a few hundreds of microns.

At present, the major limitation of FDTD and PSTD is the amount of computer resources that these techniques require. Whereas FDTD modeling of light interaction with a micron-sized, three-dimensional object can be performed on almost any personal computer, a 10-micron-size particle would require a small computer cluster. PSTD modeling of macroscopic (millimeter-scale) media is only possible with the help of state-of-the-art supercomputers. However, with more and more powerful computers and computer clusters made available, the progress in FDTD and PSTD and their applications to tissue optics are expected to increase dramatically.

8.2. Interferometric Synthetic Aperture Microscopy

Interferometric synthetic aperture microscopy (ISAM) (117–120) is a novel computed-imaging technology that is based on the coherence ranging and imaging principles of OCT and the use of synthetic aperture principles from synthetic aperture radar (SAR) (121). ISAM uses computational imaging to overcome the trade-off between depth of focus and transverse resolution. By accurately modeling the scattering processes and the data collection system, including the defocusing ignored by OCT image formation, the scattering properties of the object can be quantitatively estimated from the collected data. As in SAR, diffraction-limited resolution is achieved throughout the final image. For both ISAM and SAR, the key to this performance is the coherent collection of a complex data set.

Interferometric microscopes, such as OCT systems, provide holographic data. That is, the phase of the backscattered light can be recovered from the raw data. This is a significant advantage over standard noninterferometric systems, in which the phase information is lost at detection. This holographic data collection is analogous to the coherent data collection used in SAR systems. In both ISAM and SAR, the collection of complex coherent data allows the numerical implementation of advantageous operations that would be prohibitively difficult to implement physically. In SAR, the multiple along-track range profiles collected from a small aperture can be used to synthesize an aperture corresponding to the whole along-track path. One can envision the optical analog to this when considering a focused Gaussian beam that is transversely scanned across a point scatterer. The Gaussian beam wavefront can be decomposed into a series of plane waves, each at a different incident angle. The point scatterer will be illuminated by each of these plane waves and from many different angles as the focused Gaussian beam is translated across the point scatterer. In ISAM, these multiple complex OCT range profiles are collected, and they can be computationally reconstructed so that all planes therefore appear simultaneously in focus. The blurred, out-of-focus regions seen in OCT can therefore be brought into focus numerically (122). **Figure 7a** shows three-dimensional OCT and ISAM images of point-like titanium dioxide scatterers in a three-dimensional tissue phantom; the ISAM reconstruction clearly shows the spatially invariant focus correction throughout the volume (118).

Since the inception of ISAM, there have been studies investigating numerous practical aspects for its implementation and use. ISAM algorithms have been adapted for use not only with the Cartesian-coordinate imaging common in beam-scanned systems (118) but also for the radial-coordinate imaging found in optical catheter-based imaging systems (123). ISAM has been applied to full-field optical imaging systems (124) and systems using a spatially extended, partially coherent optical source (125), the latter of which can mitigate multiple-scattering artifacts that can arise in
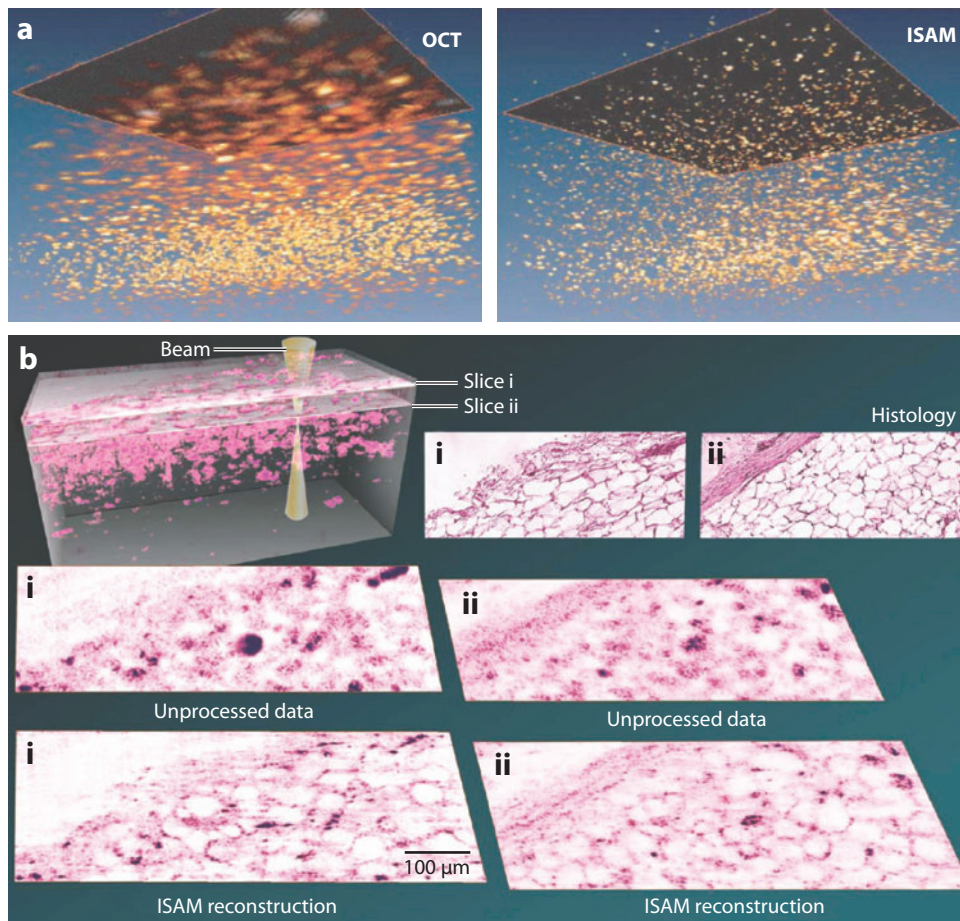
Figure 7

Interferometric synthetic aperture microscopy (ISAM). (*a*) Three-dimensional images of a tissue phantom composed of micron-sized point scatterers of titanium dioxide suspended in a gel. OCT (*left*) shows blurred, out-of-focus scatterers near the upper surface, which are corrected to the appropriate point-like objects using ISAM (*right*). (*b*) Human breast tissue. *En face* OCT images (labeled Unprocessed data) and corresponding ISAM image reconstructions from two different slices/depths within a three-dimensional block of tissue. ISAM images enable fine cellular membranes and features to be resolved. Histology sections taken from approximate locations are also shown for comparison. Adapted from Reference 118.

full-field ISAM. ISAM has also been applied to high-NA imaging systems (126), in contrast to the low-NA systems most commonly found with OCT.

The practical implementation of ISAM involves not only software algorithms but also robust and reliable hardware that can ensure phase stability in the acquired optical signals. This phase stability requirement can be met more easily with the faster acquisition capabilities of recent OCT systems employing spectral-domain detection or fast wavelength–swept sources (127, 128). The software for ISAM, also, is amenable to more efficient code that can readily enable real-time processing and display (117). Applied to biological tissue, ISAM can perform the same out-of-focus correction as was shown with the tissue phantoms, as illustrated in **Figure 7b** for human breast tissue (118).

ISAM is a computed-imaging technique that quantitatively estimates the three-dimensional scattering objects imaged with broadband coherent microscopy. The solution of the inverse problem allows for the reconstruction of areas in the sample or specimen that are typically regarded as out-of-focus and previously unusable. The result of ISAM obviates the perceived trade-off between transverse resolution and depth of focus in OCT. Although ISAM addresses an inherent weakness in OCT, namely the need to scan the focus axially to obtain images outside the original focal plane, ISAM is not merely a method to refocus the field computationally. Refocusing can be achieved from a single interferometric image at a fixed frequency, but the resulting image is still inherently two-dimensional, failing to unambiguously distinguish contributions to the image from various depths. As in other ranging technologies, the broadband nature of ISAM allows a true three-dimensional reconstruction.

ISAM and SAR are examples in the broad class of modalities known as computed imaging. Like almost all computed-imaging modalities in common practice today, they are based on the solution of linear inversion problems. The solutions to these linear inversion problems offer advantages such as the option to precompute and store the elements of an inversion kernel for rapid computation of images from data. Thus the methods take advantage of (and even rely on) one of the greatest advances in applied mathematics in the past half-century, the fast Fourier transform, which enables these computed-imaging algorithms to run fast and to be amenable to parallelization.

9. FUTURE AND EMERGING DIRECTIONS

9.1. Contrast Agents for Optical Scatter Imaging

The spectroscopic nature and high-resolution imaging capabilities of light provide a means for probing biological structure and function at the cellular and molecular levels. Although the use of fluorescent and bioluminescent probes has become a mainstay in optical molecular imaging, a large number of other optical imaging modalities would benefit from optical probes that are based on scattering, absorption, or modulation (129, 130). To this end, advances over the past several years have included a wide array of contrast agents suited for scattering-based modalities such as OCT and reflectance confocal microscopy. Most generally, these can be grouped into probes based on scattering, modulation, absorption, and plasmon-resonance effects.

Scattering probes are designed for efficient light scattering and are sensed either directly by detecting their scattered light, or indirectly through their attenuation of the incident light. To alter the intensity of the backscattered light in OCT, for example, scattering probes must introduce a local region of index-of-refraction change. One of the first demonstrations of scattering probes was the use of gold nanoparticles in electron microscopy (131) to label specific cells. In OCT, air- or gas-filled microbubbles (132) or engineered, nanoparticle-laden protein-shell microspheres (133) have been used both in cell cultures and as in vivo contrast agents introduced through the cardiovascular circulation. Because small nanoparticles have the ability to extravasate from the vascular system out toward tumor cells, many investigators have developed agents such as nanoshells or structured nanoparticles that can be either passively or actively targeted to site-specific molecular receptors, enhancing scattering-based contrast for detection (79, 134).

Detecting small localized changes in optical scattering induced by a contrast agent or probe is frequently plagued by speckle and background scattering from the tissue medium. Higher imaging specificity can therefore be achieved through the modification of an observable property of the probe in an external and controlled manner. This was achieved using magnetomotion, in which magnetic iron-oxide nanoparticles in cells or tissues are modulated with a small, external,

alternating magnetic field. The modulating nanoparticles, which are too small to exhibit a significant level of optical scattering when stationary, are displaced over several hundreds of nanometers, where they alter the local optical scattering properties of their microenvironment. Using a sensitive amplitude- and phase-resolved scattering-based detection technique such as OCT, researchers can readily detect these magnetomotive scattering signals against a highly scattering but stationary background. This technique, named magnetomotive OCT (MM-OCT), has been used to image single labeled cells (135) as well as in vivo tissue (136). Advances in phase-resolved and fast-acquisition techniques have improved sensitivity to detect ~2-nM concentrations (137). The application of magnetic fields as step-like functions causes temporally transient scattering signals to undergo underdamped oscillations, which, when analyzed, can yield quantitative biomechanical viscoelastic properties of the medium (138).

Because Rayleigh scattering theory predicts that the scattering cross section scales as the sixth power of the particle diameter, it becomes challenging to design contrast agents that are small enough for potential in vivo applications while providing sufficient scattering cross section for detection. This challenge has motivated the development of, and extensive interest in, metal nanoparticles that exhibit a collective excitation of electrons at a characteristic light frequency, a property named the surface plasmon resonance (139). At optical wavelengths, this property is primarily observable in silver and gold, the latter being particularly useful in the near-infrared wavelength region. A wide variety of surface plasmon resonance nanoparticle geometries have been investigated, including nanospheres (140), nanoshells (141), nanorods (142), and nanocages (143). These nanoparticles afford a large optical cross section while maintaining a small physical size to enable high tissue mobility. There is ongoing work to develop methods that site-specifically target these nanoparticles to molecular receptors and that use the photothermal properties of the nanoparticles to damage or kill cells for therapeutic as well as diagnostic applications.

9.2. Biological Dynamics

Dynamic time-dependent changes in optical scattering can provide a wealth of information about biological processes, in both healthy and diseased states. Dynamic changes in optical scattering can be used to enhance optical contrast in images, as discussed for magnetomotive optical scattering probes (Section 9.1). In addition, there are inherent dynamic biological processes that will vary optical scattering within cells and tissues.

9.2.1. Apoptosis. Monitoring mechanisms of programmed cell death (apoptosis) is an area of active research, as light scattering methods could ultimately be used for rapid screening of chemotherapeutic agents that act by inducing apoptosis in cancer cells. It was shown that early scattering changes within the first hour of apoptosis were consistent with an increase in the average size of subcellular scatterers and that they could be modulated by Bcl-x_L, an antiapoptosis protein that targets mitochondria (6, 33). Forward-scattering spectra and phase functions of cultured cells were also shown to change within the first hour of apoptosis in cells treated with staurosporine (42). Demonstration of scattering changes concomitant with cytochrome c release during apoptosis of photodynamically treated cells further suggests that altered light scattering by mitochondria is a significant measurable signal during apoptosis (35). Cells treated with the chemotherapeutic agent paclitaxel exhibit an increase in mass-fractal dimension, which correlates with an increase in subcellular graininess or texture, within the first 1–3 h of apoptosis and again at 12 and 24 h compared with the initial time point. The scattering changes at 1–2 h correlated with mitochondrial alterations assessed by fluorescence; changes after 6 h, with nuclear alterations (36). Elucidating these scattering changes may ultimately lead to optical-scatter-based apoptosis assays that can

track the specific time course of dynamic subcellular responses and aid in the investigation and discovery of apoptosis inducers.

9.2.2. Neuronal depolarization. Another important dynamic process investigated by light scattering is neural activity, either in single neurons or, more generally, in neural tissue. Studies using low-coherence interferometry and OCT have shown optical scattering changes in nerve fibers during the propagation of action potentials, which is understood to result from changes in nerve fiber swelling from water and ion redistribution (144, 145). Transient intrinsic scattering changes using optical coherence imaging have also been recorded from single *Aplysia californica* neurons during the firing and propagation of action potentials (146). At this scale, optical scattering changes are believed to be the result of rearrangement of membrane dipoles, producing the localized change in index of refraction (147). It has also been suggested that polarization-based scattering measurements may offer a higher sensitivity to these changes (148). Ongoing and new studies are needed to better define the biological origins and mechanisms that can be elucidated using these dynamic scattering signals not only for further insight into neural signaling but also for many other basic biological processes involving cell signaling, metabolism, and responses.

10. CONCLUSION

Light scattering spectroscopy and microscopy methods provide high sensitivity to subtle alterations in the structure and function of healthy and diseased biological tissues. The structural data obtained by optical scatter contrast can be combined with other optical modalities to characterize cellular state and structure-function relationships in cells and organelles. Furthermore, light scattering signals can report on specific time responses from tissues that can be used to monitor the effectiveness of therapeutic agents and to understand metabolism and cellular dynamics in responses to physiological and pathophysiological stimuli. Recent advances in computational methods and novel molecular probes based on optical scatter contrast have demonstrated improved optical data interpretation and image resolution. This field is advancing rapidly and promises to bring novel and effective cellular analysis and diagnostic assays.

DISCLOSURE STATEMENT

ACKNOWLEDGMENTS

LITERATURE CITED

1. Cheong WF, Prahl SA, Welch AJ. 1990. A review of the optical properties of biological tissues. *IEEE J. Quantum Electron.* 26:2166–85
2. Loudon R. 1983. *The Quantum Theory of Light*. London: Oxford Univ. Press. 393 pp. 2nd ed.
3. van de Hulst HC. 1981. *Light Scattering by Small Particles*. New York: Dover
4. Kliger DS, Lewis JW, Randall CE. 1990. *Polarized Light in Optics and Spectroscopy*. San Diego, CA: Academic. 304 pp.
5. Barer R, Tkaczyk S. 1954. Refractive index of concentrated protein solutions. *Nature* 173:821–22
6. Boustany NN, Kuo SC, Thakor NV. 2001. Optical scatter imaging: subcellular morphometry in situ with Fourier filtering. *Opt. Lett.* 26:1063–65
7. Pasternack RM, Qian Z, Zheng J, Metaxas DN, White E, Boustany NN. 2008. Measurement of subcellular texture by optical Fourier filtering with a micromirror device. *Opt. Lett.* 33:2209–11. Erratum. 2009. *Opt. Lett.* 34(13):1939
8. Itzkan I, Qiu L, Fang H, Zaman MM, Vitkin E, et al. 2007. Confocal light absorption and scattering spectroscopic microscopy monitors organelles in live cells with no exogenous labels. *Proc. Natl. Acad. Sci. USA* 104:17255–60
9. Subramanian H, Pradhan P, Liu Y, Capoglu IR, Li X, et al. 2008. Optical methodology for detecting histologically unapparent nanoscale consequences of genetic alterations in biological cells. *Proc. Natl. Acad. Sci. USA* 105:20118–23
10. Li X, Chen ZG, Taflove A, Backman V. 2004. Equiphase-sphere approximation for light scattering by stochastically inhomogeneous microparticles. *Phys. Rev. E* 70:056610
11. Li X, Taflove A, Backman V. 2005. Recent progress in exact and reduced-order modeling of light-scattering properties of complex structures. *IEEE J. Sel. Top. Quantum Electron.* 11:759–65
12. Li X, Chen ZG, Taflove A, Backman V. 2004. Equiphase-sphere approximation for analysis of light scattering by arbitrarily shaped nonspherical particles. *Appl. Opt.* 43:4497–505
13. Li X, Taflove A, Backman V. 2005. Quantitative analysis of depolarization of backscattered light by stochastically inhomogeneous dielectric particles. *Opt. Lett.* 30:902–4
14. Li X, Taflove A, Backman V. 2007. Anomalous oscillations in the spectra of light backscattered by inhomogeneous microparticles. *Phys. Rev. E* 75:037601
15. Xu M, Wu TT, Qu JY. 2008. Unified Mie and fractal scattering by cells and experimental study on application in optical characterization of cellular and subcellular structures. *J. Biomed. Opt.* 13:024015
16. Rogers JD, Capoglu IR, Backman V. 2009. Nonscalar elastic light scattering from continuous random media in the Born approximation. *Opt. Lett.* 34:1891–93
17. Capoglu IR, Rogers JD, Taflove A, Backman V. 2009. Accuracy of the Born approximation in calculating the scattering coefficient of biological continuous random media. *Opt. Lett.* 34:2679–81
18. Rajadhyaksha M, Gonzalez S, Zavislan JM, Anderson RR, Webb RH. 1999. In vivo confocal scanning laser microscopy of human skin II: advances in instrumentation and comparison with histology. *J. Invest. Dermatol.* 113:293–303
19. Fujimoto JG. 2003. Optical coherence tomography for ultrahigh resolution in vivo imaging. *Nat. Biotechnol.* 21:1361–67
20. Kuhn J, Montfort F, Colomb T, Rappaz B, Moratal C, et al. Submicrometer tomography of cells by multiple wavelength digital holographic microscopy in reflection. *Opt. Lett.* 34:653–55
21. Mertz J. 2009. *Introduction to Optical Microscopy*. Greenwood Village, CO: Roberts & Co. 413 pp.
22. Fang H, Ollero M, Vitkin E, Kimerer LM, Cipolloni PB, et al. 2003. Noninvasive sizing of subcellular organelles with light scattering spectroscopy. *IEEE J. Sel. Top. Quantum Electron.* 9:267–76
23. Popescu G, Ikeda T, Best CA, Badizadegan K, Dasari RR, Feld MS. 2005. Erythrocyte structure and dynamics quantified by Hilbert phase microscopy. *J. Biomed. Opt. Lett.* 10:060503-1–3
24. Hackenbrock CR. 1966. Ultrastructural bases for metabolically linked mechanical activity in mitochondria. I. Reversible ultrastructural changes with change in metabolic steady state in isolated liver mitochondria. *J. Cell Biol.* 30:269–97
25. Hunter DR, Haworth RA. 1979. The Ca^{2+}-induced membrane transition in mitochondria. *Arch. Biochem. Biophys.* 195:453–59

26. Bernardi P. 1992. Modulation of the mitochondrial cyclosporin A-sensitive permeability transition pore by the proton electrochemical gradient. *J. Biol. Chem.* 267:8834–39

27. Petronilli V, Constantini P, Scorrano L, Colonna R, Passamonti S, Bernardi P. 1994. The voltage sensor of the mitochondrial permeability transition pore is tuned by the oxidation-reduction state of vicinal thiols. *J. Biol. Chem.* 269:16638–42

28. Vander-Heiden MG, Chandel NS, Williamson EK, Schumacker PT, Thompson CB. 1997. Bcl-x$_L$ regulates the membrane potential and volume homeostasis of mitochondria. *Cell* 91:627–37

29. Kowaltowski AJ, Cosso RG, Campos CB, Fiskum G. 2002. Effect of Bcl-2 overexpression on mitochondrial structure and function. *J. Biol. Chem.* 277:42802–7

30. Zamzami N, Susin SA, Marchetti P, Hirsch T, Gomez-Monterrey I, et al. 1996. Mitochondrial control of nuclear apoptosis. *J. Exp. Med.* 183:1533–44

31. Mujat C, Greiner C, Baldwin A, Levitt JM, Tian F, et al. 2008. Endogenous optical biomarkers of normal and human papillomavirus immortalized epithelial cells. *Int. J. Cancer* 122:363–71

32. Smith ZJ, Berger AJ. 2008. Integrated Raman- and angular-scattering microscopy. *Opt. Lett.* 33:714–16

33. Boustany NN, Tsai YC, Pfister B, Joiner WM, Oyler GA, Thakor NV. 2004. Bcl-x$_L$-dependent light scattering by apoptotic cells. *Biophys. J.* 87:4163–71

34. Zheng J, Tsai Y, Kadimcherla P, Zhang R, Shi J, et al. 2008. The C-terminal transmembrane domain of Bcl-x$_L$ mediates changes in mitochondrial morphology. *Biophys. J.* 94:286–97

35. Wilson JD, Giesselman BR, Mitra S, Foster TH. 2007. Lysosome-damage-induced scattering changes coincide with release of cytochrome c. *Opt. Lett.* 32:2517–19

36. Chalut KJ, Ostrander JH, Giacomelli MG, Wax A. 2009. Light scattering measurements of subcellular structure provide noninvasive early detection of chemotherapy-induced apoptosis. *Cancer Res.* 69:1199–204

37. Xu C, Vinegoni C, Ralston TS, Luo W, Tan W, Boppart SA. 2006. Spectroscopic spectral-domain optical coherence microscopy. *Opt. Lett.* 31:1079–81

38. Tang S, Sun CH, Krasieva TB, Chen ZP, Tromberg BJ. 2007. Imaging subcellular scattering contrast by using combined optical coherence and multiphoton microscopy. *Opt. Lett.* 32:503–5

39. Georgakoudi I, Jacobson BC, Dam JV, Backman V, Wallace MB, et al. 2001. Fluorescence, reflectance, and light scattering spectroscopy for evaluating dysplasia in patients with Barrett's esophagus. *Gastroenterology* 120:1620–29

40. Subramanian H, Roy HK, Pradhan P, Goldberg MJ, Muldon J, et al. 2009. Nanoscale cellular changes in field carcinogenesis detected by partial wave spectroscopy. *Cancer Res.* 69:5357–63

41. Zhu Y, Fearn T, Mackenzie G, Clark B, Dunn JM, et al. 2009. Elastic scattering spectroscopy for detection of cancer risk in Barrett's esophagus: experimental and clinical validation of error removal by orthogonal subtraction for increasing accuracy. *J. Biomed. Opt.* 14:044022

42. Mulvey CS, Curtis AL, Singh SK, Bigio IJ. 2007. Elastic scattering spectroscopy as a diagnostic tool for apoptosis in cell cultures. *IEEE J. Sel. Top. Quantum Electron.* 13:1663–70

43. Wells WA, Wang X, Daghlian CP, Paulsen KD, Pogue BW. 2009. Phase contrast microscopy analysis of breast tissue differences in benign vs. malignant epithelium and stroma. *Anal. Quant. Cytol. Histol.* 31:197–207

44. Garcia-Allende PB, Krishnaswamy V, Hoopes PJ, Samkoe KS, Conde OM, Pogue BW. 2009. Automated identification of tumor microscopic morphology based on macroscopically measured scatter signatures. *J. Biomed. Opt.* 14:034034

45. Krishnaswamy V, Hoopes PJ, Samkoe KS, O'Hara JA, Hasan T, Pogue BW. 2009. Quantitative imaging of scattering changes associated with epithelial proliferation, necrosis, and fibrosis in tumors using microsampling reflectance spectroscopy. *J. Biomed. Opt.* 14:014004

46. Bartek M, Wang X, Wells W, Paulsen KD, Pogue BW. 2006. Estimation of subcellular particle size histograms with electron microscopy for prediction of optical scattering in breast tissue. *J. Biomed. Opt.* 11:06066RR

47. Abookasis D, Lay CC, Mathews MS, Linskey ME, Frostig RD, Tromberg BJ. 2009. Imaging cortical absorption, scattering, and hemodynamic response during ischemic stroke using spatially modulated near-infrared illumination. *J. Biomed. Opt.* 14:024033

48. Weber JR, Cuccia DJ, Durkin AJ, Tromberg BJ. 2009. Noncontact imaging of absorption and scattering in layered tissue using spatially modulated structured light. *J. Appl. Phys.* 105:102028

49. Amoozegar C, Giacomelli MG, Keener JD, Chalut KJ, Wax A. 2009. Experimental verification of T-matrix-based inverse light scattering analysis for assessing structure of spheroids as models of cell nuclei. *Appl. Opt.* 48(10):D20–25

50. Wax A, Pyhtila JW. 2008. In situ nuclear morphology measurements using light scattering as biomarkers of neoplastic change in animal models of carcinogenesis. *Dis. Markers* 25:291–301

51. Wilson JD, Foster TH. 2007. Characterization of lysosomal contribution to whole-cell light scattering by organelle ablation. *J. Biomed. Opt.* 12:030503

52. Cottrell WJ, Wilson JD, Foster TH. 2007. Microscope enabling multimodality imaging, angle-resolved scattering, and scattering spectroscopy. *Opt. Lett.* 32:2348–50

53. Wilson JD, Cottrell WJ, Foster TH. 2007. Index-of-refraction-dependent subcellular light scattering observed with organelle-specific dyes. *J. Biomed. Opt.* 12:014010

54. Gourley PL, Hendricks JK, McDonald AE, Copeland RG, Barrett KE, et al. 2005. Ultrafast nanolaser flow device for detecting cancer in single cells. *Biomed. Microdevices* 7:331–39

55. Smith ZJ, Berger AJ. 2009. Validation of an integrated Raman- and angular-scattering microscopy system on heterogeneous bead mixtures and single human immune cells. *Appl. Opt.* 48:D109–20

56. Gupta S, Hunter M, Kaplan D, Georgakoudi I. 2009. Optical characterization of the nanoscale organization of mineral deposits on silk films. *Appl. Opt.* 48:D45–51

57. Kim YL, Liu Y, Turzhitsky VM, Roy HK, Wali RK, Backman V. 2004. Coherent backscattering spectroscopy. *Opt. Lett.* 29:1906–8

58. Kim YL, Liu Y, Turzhitsky VM, Wali RK, Roy HK, Backman V. 2005. Depth-resolved low-coherence enhanced backscattering. *Opt. Lett.* 30:741–43

59. Kim YL, Pradhan P, Subramanian H, Liu Y, Kim MH, Backman V. 2006. Origin of low-coherence enhanced backscattering. *Opt. Lett.* 31:1459–61

60. Kim YL, Turzhitsky VM, Liu Y, Roy HK, Wali RK, et al. 2006. Low-coherence enhanced backscattering: review of principles and applications for colon cancer screening. *J. Biomed. Opt.* 11:041125

61. Kim YL, Liu Y, Wali RK, Roy HK, Backman V. 2005. Low-coherent backscattering spectroscopy for tissue characterization. *Appl. Opt.* 44:366–77

62. Roy HK, Kim YL, Liu Y, Wali RK, Goldberg MJ, et al. 2006. Risk stratification of colon carcinogenesis through enhanced backscattering spectroscopy analysis of the uninvolved colonic mucosa. *Clin. Cancer Res.* 12:961–68

63. Roy HK, Turzhitsky V, Kim Y, Goldberg MJ, Watson P, et al. 2009. Association between rectal optical signatures and colonic neoplasia: potential applications for screening. *Cancer Res.* 69:4476–83

64. Minsky M. 1961. U.S. Patent No. 3,013,467

65. Wilson T. 1990. The role of the pinhole in confocal imaging systems. In *Handbook of Biological Confocal Microscopy*, ed. JB Pawley, pp. 113–126. New York: Plenum Press

66. Gareau DS, Abeytunge S, Rajadhyaksha M. 2009. Line-scanning reflectance confocal microscopy of human skin: comparison of full-pupil and divided-pupil configurations. *Opt. Lett.* 34:3235–37

67. Shin H-J, Pierce MC, Lee D, Ra H, Solgaard O, Richards-Kortum R. 2007. Fiber-optic confocal microscope using a MEMS scanner and miniature objective lens. *Opt. Express* 15:9113–22

68. Fang H, Qiu L, Vitkin E, Zaman MM, Andersson C, et al. 2007. Confocal light absorption and scattering spectroscopic microscopy. *Appl. Opt.* 46:1760–69

69. Mishchenko MI, Travis LD, Macke A. 2000. T-matrix method and its applications. In *Light Scattering by Nonspherical Particles: Theory Measurements and Applications*, ed. MI Mishchenko, JW Hovenier, LD Travis, pp. 147–73. San Diego, CA: Academic

70. Huang D, Swanson EA, Lin CP, Schuman JS, Stinson WG, et al. 1991. Optical coherence tomography. *Science* 254:1178–91

71. Drexler W, Fujimoto JG, eds. 2008. *Optical Coherence Tomography: Technology and Applications*. Berlin: Springer-Verlag

72. Schuman JS, Puliafito CA, Fujimoto JG, eds. 2004. *Optical Coherence Tomography of Ocular Diseases*. Thorofare, NJ: SLACK Inc. 768 pp. 2nd ed.

73. Regar E, van Leeuwen TG, Serruys PW, eds. 2007. *Optical Coherence Tomography in Cardiovascular Research*. London: Informa Healthcare. 360 pp.

74. Izatt JA, Hee MR, Owen GM, Swanson EA, Fujimoto JG. 1994. Optical coherence microscopy in scattering media. *Opt. Lett.* 19:590–92

75. Morgner U, Drexler W, Kartner FX, Li XD, Pitris C, et al. 2000. Spectroscopic optical coherence tomography. *Opt. Lett.* 25:111–13

76. Oldenburg AL, Xu CY, Boppart SA. 2007. Spectroscopic optical coherence tomography and microscopy. *IEEE J. Sel. Top. Quantum Electron.* 13:1629–40

77. Xu CY, Marks DL, Do MN, Boppart SA. 2004. Separation of absorption and scattering profiles in spectroscopic optical coherence tomography using a least-squares algorithm. *Opt. Express* 12:4790–803

78. Xu CY, Ye J, Marks DL, Boppart SA. 2004. Near-infrared dyes as contrast-enhancing agents for spectroscopic optical coherence tomography. *Opt. Lett.* 29:1647–49

79. Oldenburg AL, Hansen MN, Ralston TS, Wei A, Boppart SA. 2009. Imaging gold nanorods in excised human breast carcinoma by spectroscopic optical coherence tomography. *J. Mater. Chem.* 19:6407–11

80. Xu CY, Carney PS, Boppart SA. 2005. Wavelength-dependent scattering in spectroscopic optical coherence tomography. *Opt. Express* 13:5450–62

81. Liu Y, Li X, Kim YL, Backman V. 2005. Elastic backscattering spectroscopic microscopy. *Opt. Lett.* 30:2445–47

82. Vinegoni C, Ralston T, Tan W, Luo W, Marks DL, Boppart SA. 2006. Integrated structural and functional optical imaging combining spectral-domain optical coherence and multiphoton microscopy. *Appl. Phys. Lett.* 88:053901

83. Tan W, Vinegoni C, Norman JJ, Desai TA, Boppart SA. 2007. Imaging cellular responses to mechanical stimuli within three-dimensional tissue constructs. *Microsc. Res. Tech.* 70:361–71

84. Kopp RE, Lisa J, Mendelsohn J, Pernick B, Stone H, Wohlers R. 1974. The use of coherent optical processing techniques for the automatic screening of cervical cytologic samples. *J. Histochem. Cytochem.* 22:598–604

85. Banada PP, Huff K, Bae E, Rajwa B, Aroonnual A, et al. 2009. Label-free detection of multiple bacterial pathogens using light-scattering sensor. *Biosens. Bioelectron.* 24:1685–92

86. Valentine MT, Popp AK, Weitz DA, Kaplan PD. 2001. Microscope-based static light-scattering instrument. *Opt. Lett.* 26:890–92

87. Boustany NN, Drezek R, Thakor NV. 2002. Calcium-induced alterations in mitochondrial morphology quantified in situ with optical scatter imaging. *Biophys. J.* 83:1691–700

88. Zheng J-Y, Pasternack RM, Boustany NN. 2009. Optical scatter imaging with a digital micromirror device. *Opt. Express* 17:20401–14

89. Daugman JG. 1985. Uncertainty relation for resolution in space, spatial frequency, and orientation optimized by two-dimensional visual cortical filters. *J. Opt. Soc. Am. A* 2:1160–69

90. Pasternack RM, Qian Z, Zheng J-Y, Metaxas DN, Boustany NN. 2009. Highly sensitive size discrimination of submicron objects using optical Fourier processing based on two-dimensional Gabor filters. *Opt. Express* 17:12001–12

91. Karbowski M, Norris KL, Cleland MM, Jeong S-Y, Youle RJ. 2006. Role of Bax and Bak in mitochondrial morphogenesis. *Nature* 443:658–62

92. Ramella-Roman JC, Bargo PR, Prahl SA, Jacques SL. 2003. Evaluation of spherical particle sizes with an asymmetric illumination microscope. *IEEE J. Sel. Top. Quantum Electron.* 9:301–6

93. Gabor D. 1948. A new microscope principle. *Nature* 161:777–78

94. Schnars U, Juptner W. 1994. Direct recording of holograms by a CCD target and numerical reconstruction. *Appl. Opt.* 33:179–81

95. Cuche E, Bevilacqua F, Depeursinge C. 1999. Digital holography for quantitative phase-contrast imaging. *Opt. Lett.* 24:291–93

96. Schnars U, Juptner WPO. 2002. Digital recording and numerical reconstruction of holograms. *Meas. Sci. Technol.* 13:R85–101

97. Coupland J, Lobera J. 2008. Optical tomography and digital holography. *Meas. Sci. Technol.* 19:070101

98. Popescu G, Ikeda T, Dasari RR, Feld MS. 2006. Diffraction phase microscopy for quantifying cell structure and dynamics. *Opt. Lett.* 31:775–77

99. Rockward WS, Thomas AL, Zhao B, DiMarzio CA. 2008. Quantitative phase measurements using optical quadrature microscopy. *Appl. Opt.* 47:1684–96

100. Popescu G, Park Y, Dasari RR, Badizadegan K, Feld MS. 2007. Coherence properties of red blood cell membrane motions. *Phys. Rev. E* 76:031902

101. Choi W, Fang-Yen C, Badizadegan K, Oh S, Lue N, et al. 2007. Tomographic phase microscopy. *Nat. Methods* 4:717–19

102. Jacques SL, Ramella-Roman JC. 2004. Polarized light imaging of tissues. In *Lasers and Current Optical Techniques in Biology*, ed. G Palumbo, R Pratesi, pp. 591–607. Cambridge, UK: R. Soc. Chem.

103. Oldenbourg R. 1996. A new view on polarization microscopy. *Nature* 381:811–12

104. Katoh K, Hammar K, Smith PJS, Oldenbourg R. 1999. Birefringence imaging directly reveals architectural dynamics of filamentous actin in living growth cones. *Mol. Biol. Cell* 10:197–210

105. Oldenbourg R, Salmon ED, Tran PT. 1998. Birefringence of single and bundled microtubules. *Biophys. J.* 74:645–54

106. Tower TT, Tranquillo RT. 2001. Alignment maps of tissues: II. Fast harmonic analysis for imaging. *Biophys. J.* 81:2964–71

107. Piketmay MJ, Taflove A, Troy JB. 1993. Electrodynamics of visible-light interactions with the vertebrate retinal rod. *Opt. Lett.* 18:568–70

108. Drezek R, Dunn A, Richards-Kortum R. 2000. A pulsed finite-difference time-domain (FDTD) method for calculating light scattering from biological cells over broad wavelength ranges. *Opt. Express* 6:147–57

109. Drezek R, Guillaud M, Collier T, Boiko I, Malpica A, et al. 2003. Light scattering from cervical cells throughout neoplastic progression: influence of nuclear morphology, DNA content, and chromatin texture. *J. Biomed. Opt.* 8:7–16

110. Drezek R, Dunn A, Richards-Kortum R. 1999. Light scattering from cells: finite-difference time-domain simulations and goniometric measurements. *Appl. Opt.* 38:3651–61

111. Dunn A, Richards-Kortum R. 1996. Three-dimensional computation of light scattering from cells. *IEEE J. Sel. Top. Quantum Electron.* 2:898–905

112. Chen ZG, Taflove A, Backman V. 2003. Equivalent volume-averaged light scattering behavior of randomly inhomogeneous dielectric spheres in the resonant range. *Opt. Lett.* 28:765–67

113. Li X, Chen ZG, Gong JM, Taflove A, Backman V. 2004. Analytical techniques for addressing forward and inverse problems of light scattering by irregularly shaped particles. *Opt. Lett.* 29:1239–41

114. Tseng SH, Greene JH, Taflove A, Maitland D, Backman V, Walsh J. 2004. Exact solution of Maxwell's equations for optical interactions with a macroscopic random medium. *Opt. Lett.* 29:1393–95

115. Tseng SH, Kim YL, Taflove A, Maitland D, Backman V, Walsh JT. 2005. Simulation of enhanced backscattering of light by numerically solving Maxwell's equations without heuristic approximations. *Opt. Express* 13:3666–72

116. Tseng SH, Taflove A, Maitland D, Backman V, Walsh JT. 2005. Investigation of the noise-like structures of the total scattering cross-section of random media. *Opt. Express* 13:6127–32

117. Ralston TS, Marks DL, Carney PS, Boppart SA. 2008. Real-time interferometric synthetic aperture microscopy. *Opt. Express* 16:2555–69

118. Ralston TS, Marks DL, Carney PS, Boppart SA. 2007. Interferometric synthetic aperture microscopy. *Nat. Phys.* 3:129–34

119. Davis BJ, Marks DL, Ralston TS, Carney PS, Boppart SA. 2008. Interferometric synthetic aperture microscopy: computed imaging for scanned coherent microscopy. *Sensors* 8:3903–31

120. Davis BJ, Schlachter SC, Marks DL, Ralston TS, Boppart SA, Carney PS. 2007. Nonparaxial vector-field modeling of optical coherence tomography and interferometric synthetic aperture microscopy. *J. Opt. Soc. Am. A* 24:2527–42

121. Curlander JC, McDonough RN. 1991. *Synthetic Aperture Radar: Systems and Signal Processing*. New York: Wiley-Interscience. 647 pp.

122. Ralston TS, Marks DL, Carney PS, Boppart SA. 2006. Inverse scattering for optical coherence tomography. *J. Opt. Soc. Am. A* 23:1027–37

123. Marks DL, Ralston TS, Carney PS, Boppart SA. 2006. Inverse scattering for rotationally scanned optical coherence tomography. *J. Opt. Soc. Am. A* 23:2433–39

124. Marks DL, Ralston TS, Boppart SA, Carney PS. 2007. Inverse scattering for frequency-scanned full-field optical coherence tomography. *J. Opt. Soc. Am. A* 24:1034–41

125. Marks DL, Davis BJ, Boppart SA, Carney PS. 2009. Partially coherent illumination in full-field interferometric synthetic aperture microscopy. *J. Opt. Soc. Am. A* 26:376–86

126. Ralston TS, Marks DL, Boppart SA, Carney PS. 2006. Inverse scattering for high-resolution interferometric microscopy. *Opt. Lett.* 31:3585–87

127. de Boer JF, Cense B, Park BH, Pierce MC, Tearney GJ, Bouma BE. 2003. Improved signal-to-noise ratio in spectral-domain compared with time-domain optical coherence tomography. *Opt. Lett.* 28:2067–69

128. Adler DC, Huber R, Fujimoto JG. 2007. Phase-sensitive optical coherence tomography at up to 370,000 lines per second using buffered Fourier domain mode-locked lasers. *Opt. Lett.* 32:626–28

129. Boppart SA, Oldenburg AL, Xu CY, Marks DL. 2005. Optical probes and techniques for molecular contrast enhancement in coherence imaging. *J. Biomed. Opt.* 10:041208

130. Yang C. 2005. Molecular contrast optical coherence tomography: a review. *Photochem. Photobiol.* 81:215–37

131. Horisberger M. 1981. Colloidal gold: a cytochemical marker for light and fluorescent microscopy and for transmission and scanning electron microscopy. *Scan. Electron. Microsc.* 11:9–31

132. Barton JK, Hoying JB, Sullivan CJ. 2002. Use of microbubbles as an optical coherence tomography contrast agent. *Acad. Radiol.* 9:S52–55

133. Lee TM, Oldenburg AL, Sitafalwalla S, Marks DL, Luo W, et al. 2003. Engineered microsphere contrast agents for optical coherence tomography. *Opt. Lett.* 28:1546–48

134. Sokolov K, Follen M, Aaron J, Pavlova I, Malpica A, et al. 2003. Real-time vital optical imaging of precancer using anti-epidermal growth factor receptor antibodies conjugated to gold nanoparticles. *Cancer Res.* 63:1999–2004

135. Oldenburg AL, Gunther JR, Boppart SA. 2005. Imaging magnetically labeled cells with magnetomotive optical coherence tomography. *Opt. Lett.* 30:747–49

136. Oldenburg AL, Toublan FJJ, Suslick KS, Wei A, Boppart SA. 2005. Magnetomotive contrast for in vivo optical coherence tomography. *Opt. Express* 13:6597–614

137. Oldenburg AL, Crecea V, Rinne SA, Boppart SA. 2008. Phase-resolved magnetomotive OCT for imaging nanomolar concentrations of magnetic nanoparticles in tissues. *Opt. Express* 16:11525–39

138. Crecea V, Oldenburg AL, Liang X, Ralston TS, Boppart SA. 2009. Magnetomotive nanoparticle transducers for optical rheology of viscoelastic materials. *Opt. Express* 17:23114–22

139. Wei A. 2003. Plasmonic nanomaterials. In *Nanoparticles: Scaffolds and Building Blocks*, ed. VM Rotello, pp. 173–200. New York: Kluwer Acad.

140. Chen K, Liu Y, Ameer G, Backman V. 2005. Optimal design of structured nanospheres for ultrasharp light-scattering resonances as molecular imaging multilabels. *J. Biomed. Opt.* 10:024005

141. Loo C, Lin A, Hirsch L, Lee MH, Barton J, et al. 2004. Nanoshell-enabled photonics-based imaging and therapy of cancer. *Technol. Cancer Res. Treat.* 3:33–40

142. Oldenburg AL, Hansen MN, Zweifel DA, Wei A, Boppart SA. 2006. Plasmon-resonant gold nanorods as low backscattering albedo contrast agents for optical coherence tomography. *Opt. Express* 14:6724–38

143. Chen J, Saeki F, Wiley BJ, Cang H, Cobb MJ, et al. 2005. Gold nanocages: bioconjugation and their potential use as optical imaging contrast agents. *Nano Lett.* 5:473–77

144. Lazebnik M, Marks DL, Potgieter K, Gillette R, Boppart SA. 2003. Functional optical coherence tomography for detecting neural activity through scattering changes. *Opt. Lett.* 28:1218–20

145. Fang-Yen C, Chu MC, Seung HS, Dasari RR, Feld MS. 2004. Noncontact measurement of nerve displacement during action potential with a dual-beam low-coherence interferometer. *Opt. Lett.* 29:2028–30

146. Graf BW, Ralston TS, Ko HJ, Boppart SA. 2009. Detecting intrinsic scattering changes correlated to neuron action potentials using optical coherence imaging. *Opt. Express* 17:13447–57

147. Stepnoski RA, Laporta A, Raccuiabehling F, Blonder GE, Slusher RE, Kleinfeld D. 1991. Noninvasive detection of changes in membrane-potential in cultured neurons by light-scattering. *Proc. Natl. Acad. Sci. USA* 88:9382–86

148. Yao XC, Foust A, Rector DM, Barrowes B, George JS. 2005. Cross-polarized reflected light measurement of fast optical responses associated with neural activation. *Biophys. J.* 88:4170–77

Contents

Indexes

Errata

An online log of corrections to *Annual Review of Biomedical Engineering* articles may be
found at http://bioeng.annualreviews.org/